Review | Open Access

Catalysis, Energy and Environment

Wang *et al. Catal. Energy Environ.* **2026**, *1*, 5 **DOI:**10.20517/cee.2026.13

Beyond the Haber-Bosch process: graphdiyne as an active platform for sustainable ammonia synthesis

Shitong Wang[1], Guanda Wang[1,2], Hongji Xiao[1], Haibo Wu[1], Yurui Xue[1,*]

Keywords:
Ammonia synthesis, multiscale catalysts, graphdiyne, nitrogen reduction reaction, nitrate reduction reaction

Citation: Wang, S.; Wang, G.; Xiao, H.; Wu, H.; Xue, Y. Beyond the Haber-Bosch process: graphdiyne as an active platform for sustainable ammonia synthesis. *Catal. Energy Environ.* **2026**, *1*, 5. https://dx.doi.org/10.20517/cee.2026.13

Received: 30 Jul 2026 **First Decision:** 13 Aug 2026 **Revised:** 9 Sep 2026 **Accepted:** 16 Sep 2026 **Published:** 24 Sep 2026

Academic Editor: Yongfa Zhu **Copy Editor:** Tong Wang **Production Editor:** Tong Wang

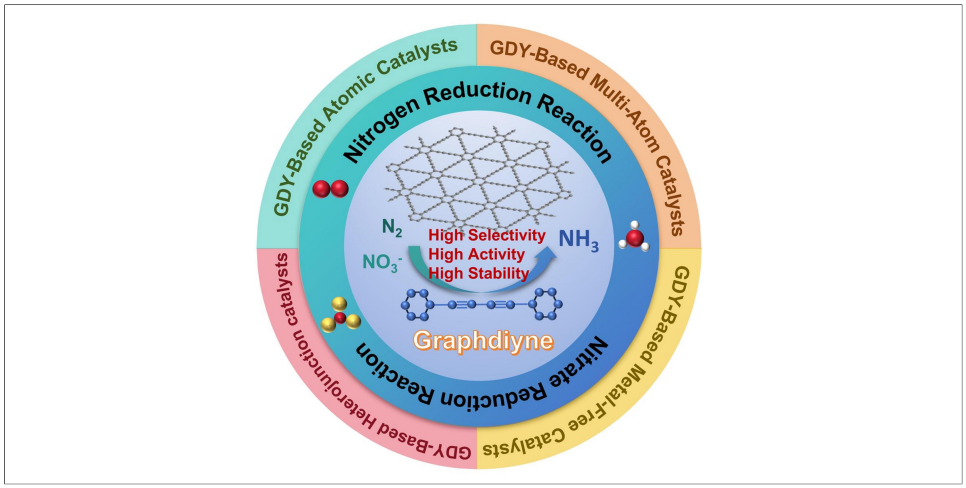

Abstract

Sustainable ammonia production under ambient conditions is a potential alternative to the fossil-fuel-dependent and CO_2-intensive Haber-Bosch route. However, the practical realization of such routes is impeded by the scarcity of catalysts capable of delivering high activity, selectivity, and durability simultaneously. Graphdiyne (GDY), a two-dimensional carbon allotrope with an intrinsically heterogeneous *sp*/*sp*^{2}-hybridized framework, has emerged as a transformative active platform to address this challenge. GDY offers unique advantages that are particularly beneficial for nitrogen fixation; for example, the noninteger charge transfer between GDY and metal atoms can stabilize unconventional zero-valent metal atoms and modulate their *d*-band centers for optimal N_2/NO_x activation. The natural alkyne-rich pore structure facilitates the assembly of active species from single atoms to clusters, maximizing site utilization and preventing aggregation. This review provides a focused and systematic analysis of GDY-based catalysts for ammonia synthesis. The design principles, including electronic modulation, spatial confinement, and interfacial synergy, that govern the construction of high-performance GDY catalysts are introduced. The applications of the catalysts in both the nitrogen reduction reaction (NRR) and nitrate reduction reaction (NtRR) are then critically discussed, with particular emphasis on the mechanistic origins of enhanced activity and suppressed competing reactions. Finally, the

[1]State Key Laboratory of Supramolecular Structure and Materials, College of Chemistry, Jilin University, Changchun 130012, Jilin, China.
[2]School of Pharmacy, Jilin University, Changchun 130012, Jilin, China.

[*]**Correspondence to:** Prof. Yurui Xue, State Key Laboratory of Supramolecular Structure and Materials, College of Chemistry, Jilin University, Changchun 130012, Jilin, China. E-mail: yrxue@jlu.edu.cn

key challenges that remain in this field are identified, and future research directions are proposed to guide the development of GDY-based catalysts toward practical and sustainable ammonia production.

INTRODUCTION

Ammonia (NH_3) stands as a cornerstone of modern industry and agriculture. As the primary feedstock for nitrogen-based fertilizers, it supports the food supply for roughly half of the world's population, while its high hydrogen content has positioned it as a leading candidate for a carbon-free energy vector[1-8]. Despite its significance, the conventional industrial NH_3 production process is extremely energy-intensive, operating under harsh conditions[9], which has intensified the search for more sustainable routes for NH_3 synthesis under milder conditions[10-16]. Electrocatalytic nitrogen reduction reaction (NRR) and nitrate reduction reaction (NtRR) using renewable electricity and water as the hydrogen source have emerged as compelling electrochemical alternatives[17-22]. However, the practical realization of these electrochemical approaches still faces many obstacles. Both processes are complex, involving multielectron, multiproton transfer processes (six electrons for the NRR to NH_3 and eight for the NtRR) and proceeding through complex intermediates (e.g., N_xH_y for the NRR; NO_2^-, NO, and N_2O for the NtRR)[23-32]. Another significant challenge is the competitive hydrogen evolution reaction (HER), which consumes electrons, thereby lowering Faradaic efficiency (FE) and decreasing overall ammonia yield[33-38]. Catalysts must be designed with atomic-level precision to activate inert nitrogenous species, stabilize key reaction intermediates, and inhibit proton reduction to boost both activity and selectivity toward NH_3.

Carbon-based materials have attracted considerable interest for nitrogen fixation, owing to their abundance, low cost, and tunable surface properties[39-42]. Nevertheless, conventional sp^2-hybridized carbon materials (such as graphene[43], carbon nanotubes[44], graphite[45]) possess electronically homogeneous surfaces[46-49]. Graphdiyne (GDY), a 2D carbon allotrope with a periodic sp-/sp^2-cohybridized network[50-53], has distinguished itself from other carbon allotropes through its intrinsic electronic heterogeneity arising from the periodic dispersion of electron-rich alkyne linkages (–C≡C–C≡C–) and electron-deficient aromatic rings[54-59]. This endows GDY with noninteger charge transfer. This, in turn, can stabilize unconventional zero-valent metal atoms and modulate their *d*-band centers, enabling precise optimization of the adsorption energy for nitrogenous intermediates[60-63]. Furthermore, *sp*-hybridized carbon atoms facilitate covalent functionalization, heteroatom doping, and organometallic coordination, providing a versatile platform to tailor the electronic structure of GDY for optimized nitrogen-fixation activity[64-67]. This integrated functionality positions GDY as a transformative catalytic platform[68].

Recent years have witnessed remarkable advancements in GDY-based catalysts for nitrogen fixation[69,70]. Various configurations, including zero-valent atom catalysts, multi-atom catalysts, quantum dots (QDs), and heterostructures, have all shown exceptional catalytic activity and selectivity for NH_3 production [Tables 1 and 2][71-100]. These findings demonstrate the crucial role of GDY in enhancing catalytic performance. Theoretical calculations and experimental characterization show that GDY plays a critical role in facilitating reactant activation, stabilizing reaction intermediates, and promoting selective protonation pathways[101,102]. Despite this rapid progress, a systematic and critical review that combines the design principles, catalytic mechanisms, and performance benchmarks of GDY-based catalysts for nitrogen fixation is lacking.

This review provides a focused and systematic analysis of GDY as an active carbon platform for selective and efficient nitrogen fixation, beginning by establishing the fundamental design principles, electronic modulation, and interfacial synergy that govern the construction of high-performance GDY-based catalysts and then critically evaluating the application of these catalysts in both the NRR and the NtRR, elucidating the mechanistic origins of enhanced activity and selectivity. This review further discusses the integration of

Table 1. Comparison of the NRR performance of GDY-based catalysts

Catalysts	Electrolyte/Conditions	Potential (V)	FE (%)	Y_{NH3}	Ref.
Mo^0/GDY	0.1 M Na_2SO_4	-1.20 V *vs.* SCE	21	145.4 $\mu g \cdot h^{-1} \cdot mg_{cat.}^{-1}$	[71]
Mo^0/GDY	0.1 M HCl	-0.1 V *vs.* SCE	15.6	2 $\mu g \cdot h^{-1} \cdot mg_{cat.}^{-1}$	[71]
Pd-GDY	0.1 M Na_2SO_4	-0.16 V *vs.* RHE	31.62 ± 1.06	4.45 ± 0.30 $mg \cdot h^{-1} \cdot mg_{Pd}^{-1}$	[72]
Pd-GDY	0.1 M HCl	-0.26 V *vs.* RHE	4.32	1,580 $\mu g \cdot h^{-1} \cdot mg_{cat.}^{-1}$	[72]
Rh SA/GDY	K_2SO_4 + H_2SO_4 (N_2, 55 atm, 25 ℃)	-0.20 V *vs.* RHE	20.36	74.15 $\mu g \cdot h^{-1} \cdot cm^{-2}$	[73]
Rh SA/GDY	K_2SO_4 + H_2SO_4 (Ambient)	-0.25 V *vs.* RHE	3.97	10.10 $\mu g \cdot h^{-1} \cdot cm^{-2}$	[73]
Ru SAs/GDY/G	0.5 M Na_2SO_4	-0.10 V *vs.* RHE	37.6	56.8 $\mu g \cdot h^{-1} \cdot mg_{cat.}^{-1}$	[74]
Ru/GDY-bAz	0.1 M K_2SO_4	-0.2 V *vs.* RHE	33.5 ± 0.5	150.2 ± 1.3 $\mu g \cdot h^{-1} \cdot mg_{cat.}^{-1}$	[75]
Ru/GDY-bNap	0.1 M K_2SO_4	-0.3 V *vs.* RHE	21.9 ± 0.5	58.3 ± 1.1 $\mu g \cdot h^{-1} \cdot mg_{cat.}^{-1}$	[75]
Re SA/GDY	0.1 M K_2SO_4 + 0.005 M H_2SO_4	-0.35 V *vs.* RHE	8.07	15.3 $\mu g \cdot h^{-1} \cdot cm^{-2}$	[76]
Mn SA/GDY	0.1 M Na_2SO_4	-0.045 V *vs.* RHE	39.83	46.78 $\mu g \cdot h^{-1} \cdot mg_{cat.}^{-1}$	[77]
Pd/HsGDY	0.05 M H_2SO_4	-0.25 V *vs.* RHE	44.45	115.93 $mg \cdot g^{-1} \cdot h^{-1}$	[78]
cFGDY	0.1 M Na_2SO_4	-1.20 V *vs.* SCE	25.95 ± 2.60	44.14 ± 4.54 $\mu g \cdot h^{-1} \cdot mg_{cat.}^{-1}$	[79]
HsGDY	0.05 M H_2SO_4	-0.20 V *vs.* RHE	5.13	103 $\mu g \cdot h^{-1} \cdot mg_{cat.}^{-1}$	[80]
Cl-GDY	0.1 M HCl	-0.40 V *vs.* RHE	8.7	10.7 $\mu g \cdot h^{-1} \cdot cm^{-2}$	[81]
IVR-FO/GDY	0.1 M Na_2SO_4	+0.255 V *vs.* RHE	59.48 ± 2.57	127.9 ± 9.11 $\mu g \cdot h^{-1} \cdot mg_{cat.}^{-1}$	[82]
GDY/Co_2N	0.1 M Na_2SO_4	+0.055 V *vs.* RHE	35.84	123.66 $\mu g \cdot h^{-1} \cdot mg_{cat.}^{-1}$	[83]
GDY/Co_2N	0.1 M HCl	+0.101 V *vs.* RHE	58.60	219.72 $\mu g \cdot h^{-1} \cdot mg_{cat.}^{-1}$	[83]
Mo_1/HsGDY@Cu_2O	0.01 M PBS (AM 1.5 G, 100 $mW \cdot cm^{-2}$)	0 V *vs.* RHE	42.8	15.8 $\mu g \cdot h^{-1} \cdot cm^{-2}$	[84]

NRR: Nitrogen reduction reaction; GDY: graphdiyne; SCE: saturated calomel electrode; RHE: reversible hydrogen electrode.

Table 2. Comparison of the NtRR performance of GDY-based catalysts

Catalysts	Electrolyte	Potential (V)	FE (%)	Y_{NH3}	Ref.
Cu/Cu_xO/GDY	1.0 M KOH + 0.1 M KNO_3	-0.80 V *vs.* RHE	99.8	25.4 $mg \cdot h^{-1} \cdot mg_{cat.}^{-1}$	[85]
$PtCu_x$/GDY	1.0 M KOH + 0.1 M KNO_3	-0.50 V *vs.* RHE	96.5 ± 5.1	345.3 ± 38.9 $\mu mol \cdot h^{-1} \cdot cm^{-2}$	[86]
Pd/GDY-F	0.1 M KOH + 0.1 M NO_3^-	-0.7 V *vs.* RHE	74.9 ± 1.8	2,812.8 ± 40.8 $\mu g \cdot h^{-1} \cdot mg_{cat.}^{-1}$	[87]
Cu^0/GDYNA	0.1 M NO_3^- + 0.5 M SO_4^{2-}	-2.0 V *vs.* SCE	81.25	15.45 $mmol \cdot h^{-1} \cdot cm^{-2}$	[88]
Cu_3N/GDY	1.0 M KOH + 0.1 M KNO_3	-0.90 V *vs.* RHE	98.1	35,280 $\mu g \cdot h^{-1} \cdot mg_{cat.}^{-1}$	[89]
Cu_2O/GDY	1.0 M KOH + 0.1 M KNO_3	-1.70 V *vs.* Hg/HgO	94	26,997 $\mu g \cdot h^{-1} \cdot mg_{cat.}^{-1}$	[90]
Cu_xO/N-GDY	1.0 M KOH + 0.1 M KNO_3	-0.50 V *vs.* RHE	89	340 $\mu mol \cdot h^{-1} \cdot mg_{cat.}^{-1}$	[91]
$CuCo_2O_x$/GDY	1.0 M KOH + 0.1 M NO_3^-	-0.132 V *vs.* RHE	≈100	3332 $\mu mol \cdot h^{-1} \cdot cm^{-2}$	[92]
Co_3O_4/GDY	0.5 M K_2SO_4 + 0.1 M KNO_3	-1.05 V *vs.* RHE	92.45	0.78 $mmol \cdot h^{-1} \cdot cm^{-2}$	[93]
Fe_3C@GDY	0.1 M K_2SO_4 + 0.01 M NO_3^-	-0.6 V *vs.* RHE	96.8	205.57 $\mu mol \cdot h^{-1} \cdot cm^{-2}$	[94]
GDY-MnO_x	0.1 M KOH + 0.1 M NO_3^-	-0.891 V *vs.* RHE	95.4	463.4 $\mu mol \cdot h^{-1} \cdot cm^{-2}$	[95]
ZIFNC@GDY	0.1 M NO_3^- + 0.5 M SO_4^{2-}	-0.745 V *vs.* RHE	98.51 ± 0.75	0.40 ± 0.02 $mmol \cdot h^{-1} \cdot cm^{-2}$	[96]
NiBDC@HsGDY@Cu	1.0 M KOH + 0.1 M KNO_3	-0.11 V *vs.* RHE	95.5	0.321 $mmol \cdot h^{-1} \cdot cm^{-2}$	[97]
NiCoBDC@HsGDY	1.0 M KOH + 0.1 M NO_3^-	-0.34 V *vs.* RHE	99.1	0.56 $mmol \cdot h^{-1} \cdot cm^{-2}$	[98]
h-FeCoNiPBA@GDY	0.5 M KNO_3 + 1.0 M KOH	-0.432 V *vs.* RHE	95.10	1,015.5 $\mu mol \cdot h^{-1} \cdot cm^{-2}$	[99]
$Cu_3(BTC)_2$@HsGDY	200 ppm NO_3^- + 0.5 M SO_4^{2-}	-0.7 V *vs.* RHE	95.10	1.016 $mmol \cdot h^{-1} \cdot cm^{-2}$	[100]

NtRR: Nitrate reduction reaction; GDY: graphdiyne; SCE: saturated calomel electrode; RHE: reversible hydrogen electrode.

GDY-based catalysts into practical electrochemical systems and emerging directions such as photocatalytic nitrogen fixation. Finally, the remaining challenges in scalable synthesis, operational stability under industrially relevant conditions, and the need for advanced operando characterization are discussed, and roadmaps are proposed to guide the transition of GDY-based nitrogen-fixation catalysts from fundamental breakthroughs to practical, sustainable ammonia production.

DESIGN PRINCIPLES OF GDY-BASED CATALYSTS FOR NITROGEN FIXATION

Electronic modulation, spatial confinement, and interfacial synergy are not independent but synergistically integrated within the unique *sp*/*sp*^{2}-cohybridized structure of GDY to efficiently catalyze ammonia production. This integrated functionality positions GDY as an ideal platform that actively participates in catalytic turnover through multiple, interconnected mechanisms rather than passively supporting active species, and provides a systematic framework for rational catalyst design[54,103-107]. This section elaborates on each principle, establishing the mechanistic foundation for the catalytic applications discussed in subsequent sections.

Electronic modulation via noninteger charge transfer

The fundamental and distinguishing feature of GDY as a catalytic platform is its ability to engage in noninteger charge transfer with anchored metal atoms[108]. This capability arises directly from GDY's intrinsic electronic heterogeneity of the periodic alternation of electron-rich alkyne linkages (–C≡C-C≡C–) and electron-deficient aromatic rings, which creates a spatially varying electrostatic potential that facilitates bidirectional electron exchange with anchored atoms. The alkyne domains of GDY actively participate in electronic communication with metal species[106,109-111]. The electron-rich *sp*-hybridized carbon atoms donate electron density to incoming metal atoms while accepting back-donation from the metal's *d*-orbitals. This synergistic charge transfer stabilizes metal atoms in unconventional zero-valent states, a configuration that maximizes *d*-electron availability for catalytic turnover while preventing aggregation into larger clusters or nanoparticles[112-114].

Through efficient charge transfer, the *d*-band center of anchored metal atoms can be precisely modulated to achieve optimal binding strength for nitrogenous intermediates, thereby facilitating N_2/NO_3^- activation and the release of NH_3. Such electronic tunability is unattainable on electronically homogeneous *sp*^{2}-carbon surfaces.

This electronic modulation principle has been demonstrated across a wide range of metal species. Theoretical screening has identified numerous transition metal atom catalysts (TM@GDY) with tailored *d*-band centers for nitrogen reduction. Experimentally, zero-valent metal atoms of Pd[72], Pt[115], Ru[74], Rh[73], Os[116], Mo[71], Fe[117], Co[118], and Ni[117] have all been successfully stabilized on GDY through noninteger charge transfer. The extent of charge transfer can be further tuned by varying the metal identity, GDY thickness, or the introduction of substituent groups, providing a versatile platform for optimizing catalytic activity and selectivity across different nitrogen-fixation reactions. Beyond single atoms, unique noninteger charge transfer also extends to dual-atom catalysts (DACs), QD catalysts, and heterostructured catalysts. These reported catalysts all exhibit enhanced catalytic performance through cooperative electron transfer.

Spatial confinement effect of natural pores

GDY possesses natural triangular pores with a radius of approximately 0.45 nm[101,119,120]. These nanopores can also serve as geometrically matched cages that impose spatial confinement on deposited metal species and simultaneously modulate their local electronic environment. For example, triangular pores are ideally sized to accommodate isolated metal atoms, preventing their migration and coalescence even under harsh electrochemical conditions[121-123]. This restricts the free movement and volume change of the anchored

species, ensuring high active-site stability and maximizing the atom-utilization efficiency, which are the critical requirements for efficient catalysis[101]. Owing to these advantages, the extended 2D surface of GDY can direct the growth of QDs, clusters, and heterostructures with controlled size, crystallinity, and dispersion.

Importantly, the spatial confinement effect is not merely passive but also synergistically coupled with electronic modulation. Density functional theory (DFT) calculations show that transition metal atoms and clusters anchored within the triangular pores of GDY exhibit high adsorption energies, indicating the stability of these catalytic systems[124]. Experimentally, researchers have achieved controlled growth of active sites on GDY by exploiting the confinement effect. Such spatial and electronic dual confinement of GDY creates a unique catalytic microenvironment that cannot be replicated on open surfaces or in larger pores[55,103]. For nitrogen fixation applications, this capability enables rational catalyst design with precisely defined active-site architectures, from isolated single atoms to closely spaced dual atoms and clusters, for selective N_2 or NO_3^- activation and NH_3 formation.

Interfacial synergy in heterostructures

Another important design principle extends beyond the GDY itself to the interfaces formed between the GDY and metal nanostructures. The chemical addressability of GDY, enabled by its *sp*-hybridized carbon atoms, allows for seamless integration with a diverse range of materials, from transition metal dichalcogenides (TMDs) to metal oxides, nitrides, and metal-organic frameworks (MOFs)[97,125]. The resulting heterointerfaces exhibit synergistic effects that are unavailable in single-component systems, including heterointerface charge redistribution that drives electron transfer across the interface, creating an internal electric field that facilitates charge separation and enhances catalytic kinetics[68]. For nitrogen fixation, interfacial charge transfer can optimize the adsorption energetics of nitrogenous intermediates on the active sites. For example, the GDY/Co_2N[83] interface has been shown to facilitate preferential N_2 adsorption at coordinatively unsaturated Co sites, whereas alkyne C-sites redistribute H-species to suppress the competing HER. In addition, the lattice strain effect at GDY heterointerfaces can continuously tune the electronic structure of the active sites, shifting *d*-band centers and modifying adsorption energetics. The magnitude of strain can be systematically controlled by varying the GDY layer thickness or the heterostructure partner, providing a tunable parameter for optimizing catalytic performance. Strain engineering offers an additional lever for fine-tuning the binding strength of N_2, NO_3^-, and reaction intermediates to achieve the optimal balance between activation and product release during the nitrogen fixation process.

GDY-based Catalysts for NRRs

Atom catalysts on GDY

Atomic catalysts (ACs) represent a new frontier in catalysis and are defined as catalysts consisting of zero-valent metal atoms that are atomically dispersed and anchored on supporting materials[126-128]. This architectural paradigm maximizes metal atom utilization efficiency, approaching the theoretical limit of 100%, while offering unique electronic and geometric properties that are unattainable with conventional nanoparticles or clusters[129-131]. However, traditional single-atom catalysts face persistent challenges in terms of the migration and aggregation of metal atoms, and conventional synthesis methods lack precision in controlling the chemical structure and charge distribution of individual metal atoms. These limitations seriously impede the understanding of structure-activity relationships and catalytic mechanisms at the atomic level[35,132-134]. The unique *sp*/sp^2-carbon framework and the confinement effects resulting from the uniform acetylenic cavities and strong noninteger charge transfer between metal atoms and GDY enable effective and precise single-metal-atom stabilization[135-137]. Unlike N-doped carbon substrates, the neutral C≡C bonds in GDY tend to stabilize zero-valent or low-valence transition metals[138]. This electronic regulation simultaneously activates the N≡N triple bond via M-to-N_2 π-backdonation and optimizes *p*-*d* orbital coupling while restraining competitive HER, thus increasing both selectivity and catalytic activity in electrochemical NRR.

In 2019, Hui *et al.* reported the first zero-valent molybdenum-atom catalyst (Mo^0/GDY) with a high metal loading of 7.5 wt% for ammonia synthesis from the reduction of nitrogen[71]. The structural configurations of Mo^0/GDY at different reaction stages are shown in Figure 1A. High-angle annular dark field imaging in the aberration-corrected scanning transmission electron microscope (HAADF-STEM) and X-ray absorption near edge strucure (XANES) confirm the anchoring of individual Mo^0 atoms at the alkyne ring corners of GDY [Figure 1B and C]. For example, Mo^0/GDY achieved a maximum FE exceeding 21% and an ammonia yield rate (Y_{NH_3}) of 145.4 $\mu g \cdot h^{-1} \cdot mg_{cat.}^{-1}$ at -1.2 V *vs.* saturated calomel electrode (SCE) in neutral 0.1 M Na_2SO_4 [Figure 1D]. More recently, Yu *et al.* reported the spontaneous anchoring of zero-valent single palladium atoms supported on GDY (Pd-GDY) for the electrocatalytic NRR [Figure 1E][72]. HAADF-STEM images confirm the atomic dispersion of isolated Pd atoms on GDY [Figure 1F]. In addition, XANES clearly shows that Pd atoms in Pd-GDY are in a zero-valent state [Figure 1G]. This unique property of GDY endows the catalyst with excellent NRR activity and durability. In 0.1 M Na_2SO_4, Pd-GDY achieved an optimal Y_{NH_3} of 4.45 ± 0.30 mg_{NH_3} $mg_{Pd}^{-1} \cdot h^{-1}$ and an FE of 31.62% at -0.16 V *vs.* reversible hydrogen electrode (RHE) [Figure 1H], as well as durability over consecutive recycling tests. Zou *et al.* reported a one-pot stereo-confinement strategy to anchor high-loading transition metal atoms (Rh, Ru, and Co) on GDY using C-C cross-coupling and reductive elimination to entrap metal single atoms on GDY [Figure 1I]. HAADF-STEM images confirmed the dense atomic dispersion of the metal atoms [Figure 1J]. Their experimental results revealed that a high partial pressure (55 atm N_2) could significantly increase N_2 solubility and the thermodynamic driving force while effectively retarding the HER for the NRR. Among the synthesized catalysts, Rh single atom anchored on GDY (Rh SA/GDY) achieved an exceptional Y_{NH_3} of 74.15 $\mu g \cdot h^{-1} \cdot cm^{-2}$, an FE of 20.36%, an NH_3 partial current density (j_{NH_3}) of 0.35 $mA \cdot cm^{-2}$ at -0.20 V *vs.* RHE [Figure 1K and L], and high cycling stability[73].

Recently, researchers have investigated the durability and distinctive characteristics of zero-valent single-atom catalysts. Feng *et al.* designed a Ru single-atom catalyst supported on a graphdiyne/graphene sandwich architecture (Ru SAs/GDY/G)[74]. At a low potential of -0.1 V *vs.* RHE, the catalyst delivered a remarkable NH_3 yield rate of 56.8 $\mu g \cdot h^{-1} \cdot mg_{cat.}^{-1}$ (4.7 $mg \cdot h^{-1} \cdot mg_{Ru}^{-1}$), with a FE of 37.6%. GDY not only suppresses hydrogen coverage at Ru single-atom sites, thereby minimizing the competitive HER, but also generates hydrogen radicals (H·), accelerating the hydrogenation kinetics of the NRR. Notably, this hydrogen radical transfer (H·-transfer) pathway represents a novel mechanistic discovery in the electrocatalytic NRR [Figure 1M-P]. In addition, Mn SA/GDY exhibits efficient NH_3 synthesis under ambient conditions, delivering a production rate of 46.78 $\mu g \cdot h^{-1} \cdot mg_{cat.}^{-1}$ and a FE of 39.83%[77]. Zou *et al.* reported that the NRR performance of atom catalysts on GDY (M SA/GDY; M = Cr, Mo, W, Mn, and Re) decreased in the order Re > Mo > Cr > W > Mn[76]. Strong M-to-N_2 *pi*-backdonation on Re SA/GDY lowers the free-energy input for the potential-determining stage (*N_2 to *NNH) to +0.39 eV, establishing an N_2/H_2O-assisted ligand-exchange mechanism for facile NH_3 desorption with a low energy requirement of +0.83 eV. Xiong *et al.* demonstrate that GDY-supported uranium single atoms (U/GDY) leverage the unique electronic properties and f-orbital interactions of actinide sites to effectively promote N_2 coordination and N≡N bond activation[139].

Collectively, these studies reveal that GDY, with a unique sp/sp^2-hybridized framework and intrinsic noninteger charge-transfer capability, serves as an exceptional platform for stabilizing zero-valent single atoms across a broad range of transition metals and even actinides. Precise control over metal coordination environments, combined with the electronic modulation enabled by GDY's alkyne-rich cavities, not only optimizes reactant activation and hydrogenation kinetics but also effectively suppresses the competing HER. This atomic-level catalyst design paradigm offers a versatile, robust strategy for high catalytic performance, paving the way for the rational development of next-generation single-atom catalysts for sustainable ammonia synthesis.

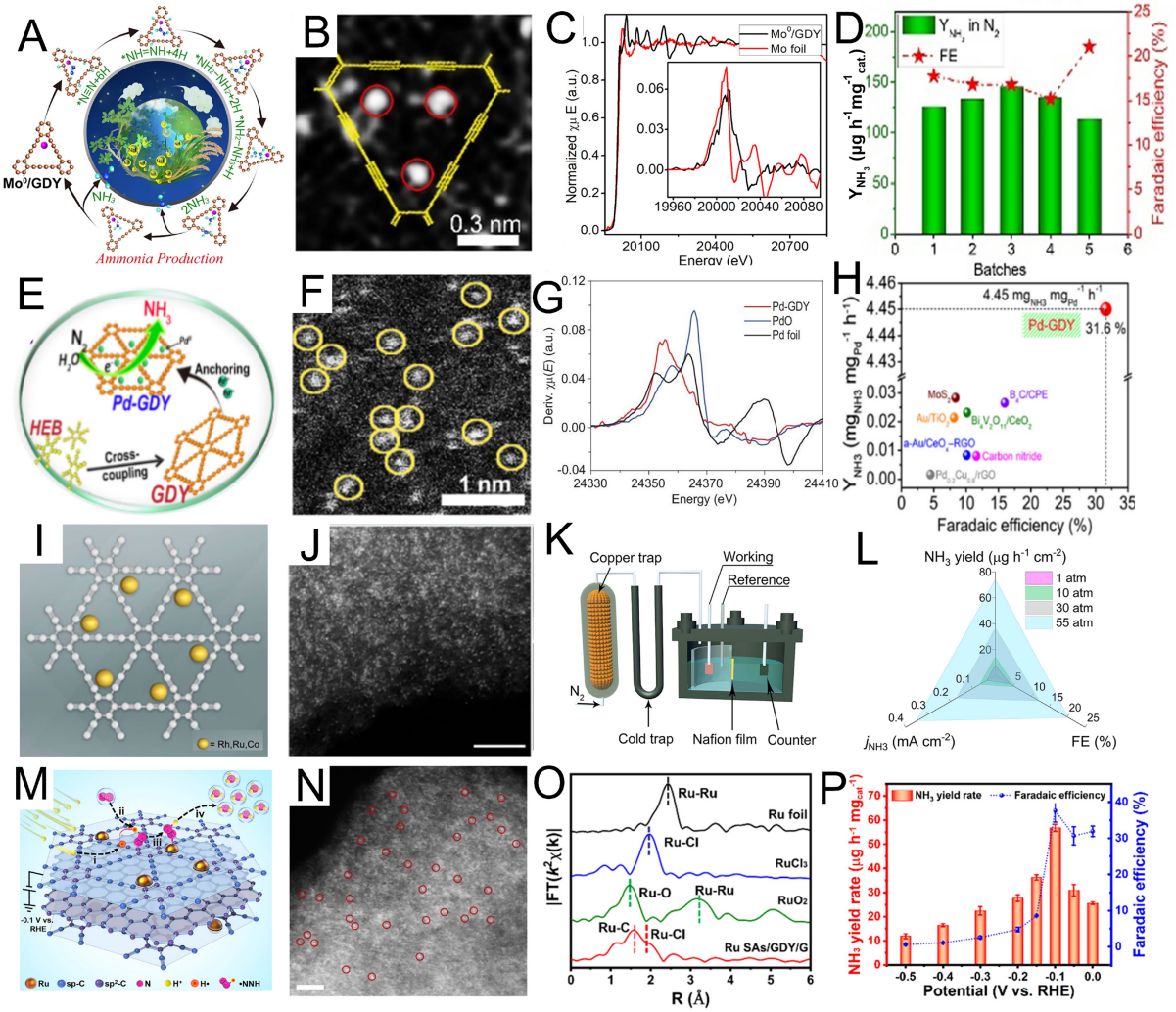

Figure 1. (A) Mo^0/GDY structural evolution during catalysis; (B) HAADF-STEM image of Mo^0/GDY samples; (C) Mo K-edge XANES profiles of Mo^0/GDY and Mo foil (inset: derived first derivative curves); (D) NH_3 production performance for different batches of Mo^0/GDY[71]; (A-D) are reprinted with permission from reference[71]. Copyright 2019 American Chemical Society; (E) Pd-GDY catalyst synthesis schematic; (F) HAADF-STEM results of Pd-GDY; (G) First derivative curves of Pd K-edge XANES spectra for Pd-GDY, PdO, and Pd foil; (H) Comparison of the catalytic performance of Pd-GDY with reported catalysts[72]; (E-H) are reprinted with permission from reference[72]. Reproduced under the CC BY license; (I) Schematic illustration of M SA/GDY (M = Rh, Ru, and Co); (J) HAADF-STEM image of Rh SA/GDY; (K) Schematic of the homemade pressurized NRR setup; (L) Performance comparison of Rh SA/GDY at different applied N_2 pressures[73]; (I-L) are reprinted with permission from reference[73]. Reproduced under the CC BY license; (M) NRR process on Ru SAs/GDY/G; (N) Imaging of Ru SAs/GDY/G by HAADF-STEM. Some Ru single atoms are highlighted with red rings; (O) FT k^2-weighted $\chi^{(k)}$ function of the EXAFS spectra at the Ru K-edge of Ru SAs/GDY/G, Ru foil, $RuCl_3$, and RuO_2; (P) Catalytic performance of Ru SAs/GDY/G at different potentials[74]; (M-P) are reprinted with permission from reference[74]. Copyright 2023 American Chemical Society. GDY: Graphdiyne; HEB: hexaethynylbenzene; RHE: reversible hydrogen electrode; HAADF-STEM: high-angle annular dark field imaging in the aberration-corrected scanning transmission electron microscope; XANES: X-ray absorption near edge strucure; SA: single atom; NRR: nitrogen reduction reaction; FT: Fourier transform.

GDY-based multi-atom catalysts for NRR

While single-atom catalysts offer maximized atom utilization and well-defined active sites, they are inherently limited by the linear scaling relations (LSRs) that govern the adsorption energies of reaction intermediates on single metal centers[140,141]. In the context of the NRR, this limitation manifests as competition between N_2 activation/hydrogenation and NH_3 desorption, which demand opposite binding

strengths, thereby imposing a thermodynamic ceiling on the achievable activity and selectivity. Multi-atom catalysts provide a compelling strategy to overcome this limitation by introducing proximal metal centers that can cooperatively bind and transform nitrogenous species, effectively decoupling the scaling constraints inherent to single-site catalysis[142].

A representative demonstration of this cooperative effect comes from Guo *et al.*, who synthesized subnanometer Pd clusters supported on hydrogen-substituted GDY (Pd/HsGDY)[78] [Figure 2A-E]. Their results showed that the electron-withdrawing diacetylene units in HsGDY shift the *d*-band center of Pd clusters downward, preventing overbinding of nitrogen reaction intermediates and accelerating N-hydrogenation kinetics, leading to high FE (44.45%) and an NH_3 yield rate (115.93 $mg_{cat}^{-1}·h^{-1}$).

Extending this concept to heteronuclear dual-atom systems, theoretical studies have demonstrated that GDY can function as a dynamic electron reservoir, shuttling charge through metal bridges to adsorbed N_xH_y intermediates and thereby breaking conventional scaling restrictions between $*N_2H$ and $*NH_2$ species [Figure 2F]. Systematic DFT screening of vanadium-paired transition metals of the 3d series on GDY (V-TM@GDY) revealed a volcano-type correlation between N_2 charge transfer ($Q(N_2)$) and the limiting potential. V-Cr@GDY and V-Fe@GDY achieve exceptionally low limiting potentials (-0.36 and -0.42 V) alongside a theoretical FE of nearly 100% for NH3[143]. Free-energy profile evaluations for Co-Ni@GDY (distal mechanism, U_L = -0.52 V) and Mo_2@GDY (consecutive mechanism, U_L = -0.61 V) further confirm that dual-atom bridging sites provide the coordination flexibility to optimize intermediate binding and lower reaction barriers[147]. Another pivotal insight emerges from comparative studies on homonuclear (Co_2@GDY[148], Fe_2@GDY[145], and Mo_2@GDY[145]) and heteronuclear (FeCo@GDY and NiCo@GDY[145], and Rh-Hf@GDY and Rh-Ta@GDY[144]) dimers [Figure 2G-I], which highlight the decisive role of the metal interatomic distance (~2.4-2.6 Å) in determining the N_2 adsorption geometry. Optimal interatomic spacing promotes side-on N_2 chemisorption, enabling simultaneous two-center electron donation/backdonation to elongate the N≡N bond and lower the initial hydrogenation barrier ($\Delta G_{*N_2 \rightarrow *NNH}$).

Pushing the boundary toward higher nuclearity, investigations into Mo_3@GDY[149], Fe_3-GDY[150] and Ti-Co_3@GDY[146] catalysts reveal that triatomic hollow sites achieve ultrahigh mass loading while expertly balancing reactant activation and product release, with limiting potentials between -0.26 and -0.32 V [Figure 2J]. Notably, this multinuclear synergy is not confined to metallic systems. In the nonmetallic domain, double boron-doped GDY (GDY-2B[151]) exemplifies a dual-Lewis-acid "pull-pull" mechanism that traps N_2 lone pairs, achieving an overpotential as low as 0.12 V. Theoretical simulations confirm the stable incorporation of S and N atoms into the GDY monolayer (GDY@SN), yielding structurally robust doped frameworks with tunable electronic properties for NRR[152]. This multinuclear strategy defines a robust framework for the design of efficient electrocatalytic nitrogen conversion systems.

These studies demonstrate that GDY-based multi-atom catalysts effectively circumvent the intrinsic scaling limitations of single-site catalysis through the synergistic interaction of adjacent metal sites. Continued exploration of GDY-supported multi-atom architectures, through integrated computational screening and precision synthesis, holds great promise for unlocking next-generation catalysts toward sustainable and scalable ammonia production.

Metal-free GDY and heteroatom-doped GDY

In addition to serving as a support for metal-based catalysts, GDY and its derivatives can also be used as metal-free catalysts with high intrinsic activity for NRR. This is particularly attractive from the perspectives of cost, sustainability, and scalability. This section summarizes the strategies for realizing and enhancing metal-free NRRs on GDY-based platforms, including H[80], N[153,154], O[155], B[156], F[79], or Cl-doped graphdiyne [81].

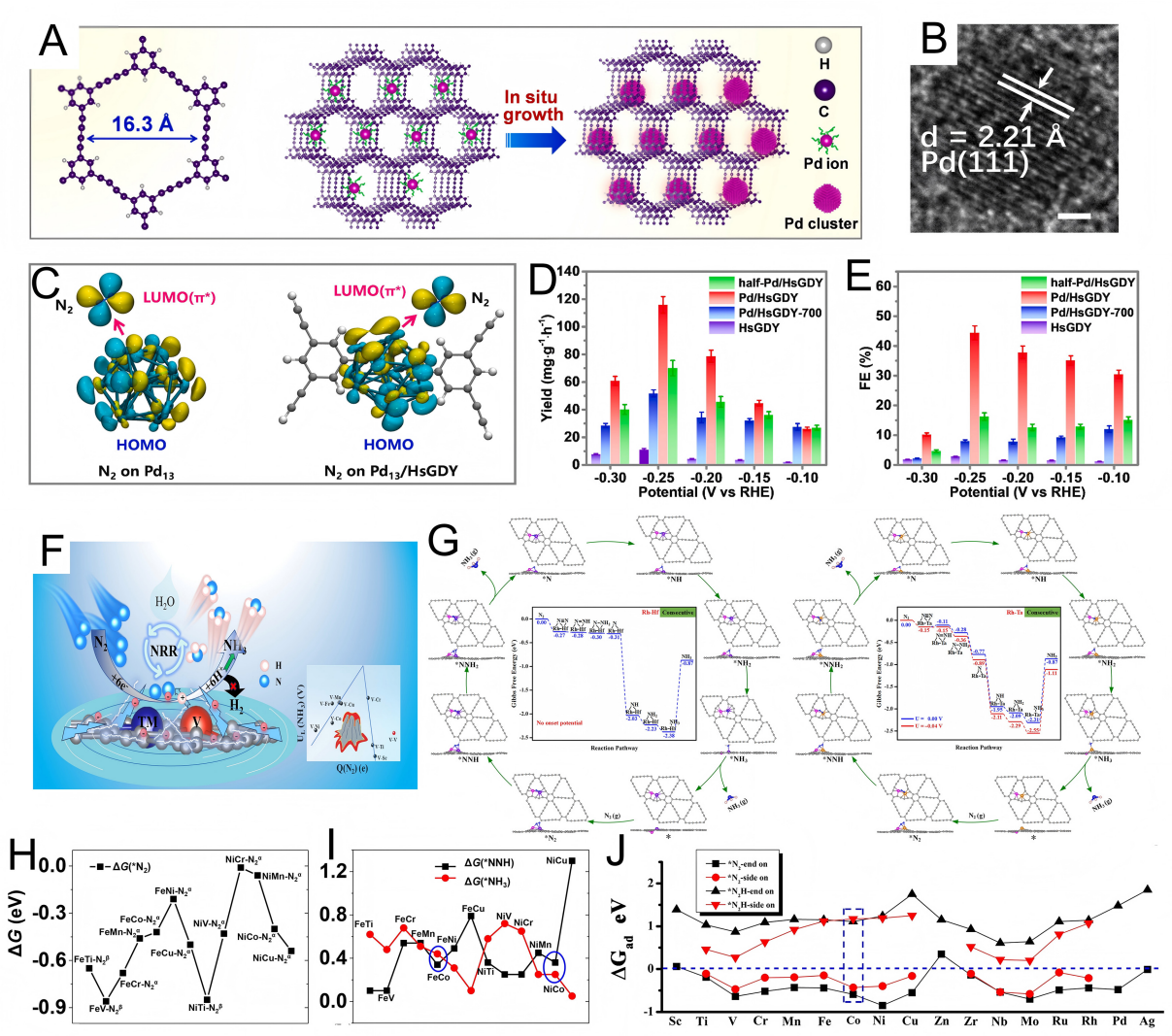

Figure 2. (A) The structural feature of HsGDY, along with a schematic depiction of the preparation route for Pd/HsGDY; (B) HRTEM of Pd/HsGDY; (C) N_2 adsorption on Pd_{13} and Pd_{13}/HsGDY; pink arrows denote electron-transfer direction; (D and E) NH_3 yields and FEs for the catalysts[78]; (A-E) are reprinted with permission from reference[78]. Copyright 2021 Elsevier; (F) Dual-atom catalysts composed of V and 3d TMs have enhanced NRR activity because they modulate charge transfer[143]. Reprinted with permission from reference[143]. Copyright 2025 The Royal Society of Chemistry; (G) Gibbs free-energy profiles and intermediate geometries along optimal routes on Rh-Hf@GDY and Rh-Ta@GDY at zero (blue) and onset (red) potentials, respectively[144]. Reprinted with permission from reference[144]. Reproduced under the CC BY license; (H) Free-energy changes for the best N_2 adsorption on tested catalysts ($\Delta G(N_2)$), with N_2^{α} and N_2^{β} representing end-on and side-on adsorption; (I) ΔG(NNH) and $\Delta G(*NH_3)$ correspond to the first and last proton-electron pair transfers to N_2 (forming NNH) and NH_2 (forming NH_3), respectively[145]; (H and I) are reprinted with permission from reference[145]. Copyright 2020 Science Press and Dalian Institute of Chemical Physics, Chinese Academy of Sciences. Published by Elsevier B.V. and Science Press; (J) Adsorption energies of N_2 and N_2H in the end-on and side-on patterns on TM-Co_3@GDY[146]. Reprinted with permission from reference[146]. Copyright 2021 American Chemical Society. LUMO: Lowest unoccupied molecular orbital; HOMO: highest occupied molecular orbital; HsGDY: hydrogen-substituted graphdiyne; RHE: reversible hydrogen electrode; FEs: Faraday efficiencies; TMs: Sc, Ti, V, Cr, Mn, Fe, Co, Ni, Cu, Zn, Zr, Nb, Mo, Ru, Rh, Pd, and Ag, toxic/radioactive elements were excluded in this study; NRR: nitrogen reduction reaction; NNH: *NNH free radical; HRTEM: high-resolution transmission electron microscopy.

HsGDY features a fully conjugated *sp*/*sp*^{2} carbon network[157]. The localized electron polarization on its inner alkynyl carbon chain lowers the activation barrier for key hydrogenation steps, particularly the NH_2NH_2 formation, while inherently suppressing the competing HER. Xing *et al.* successfully synthesized crystalline fluorinated GDY (cFGDY) with a 9-fold stacking mode, as confirmed by high resolution transmission

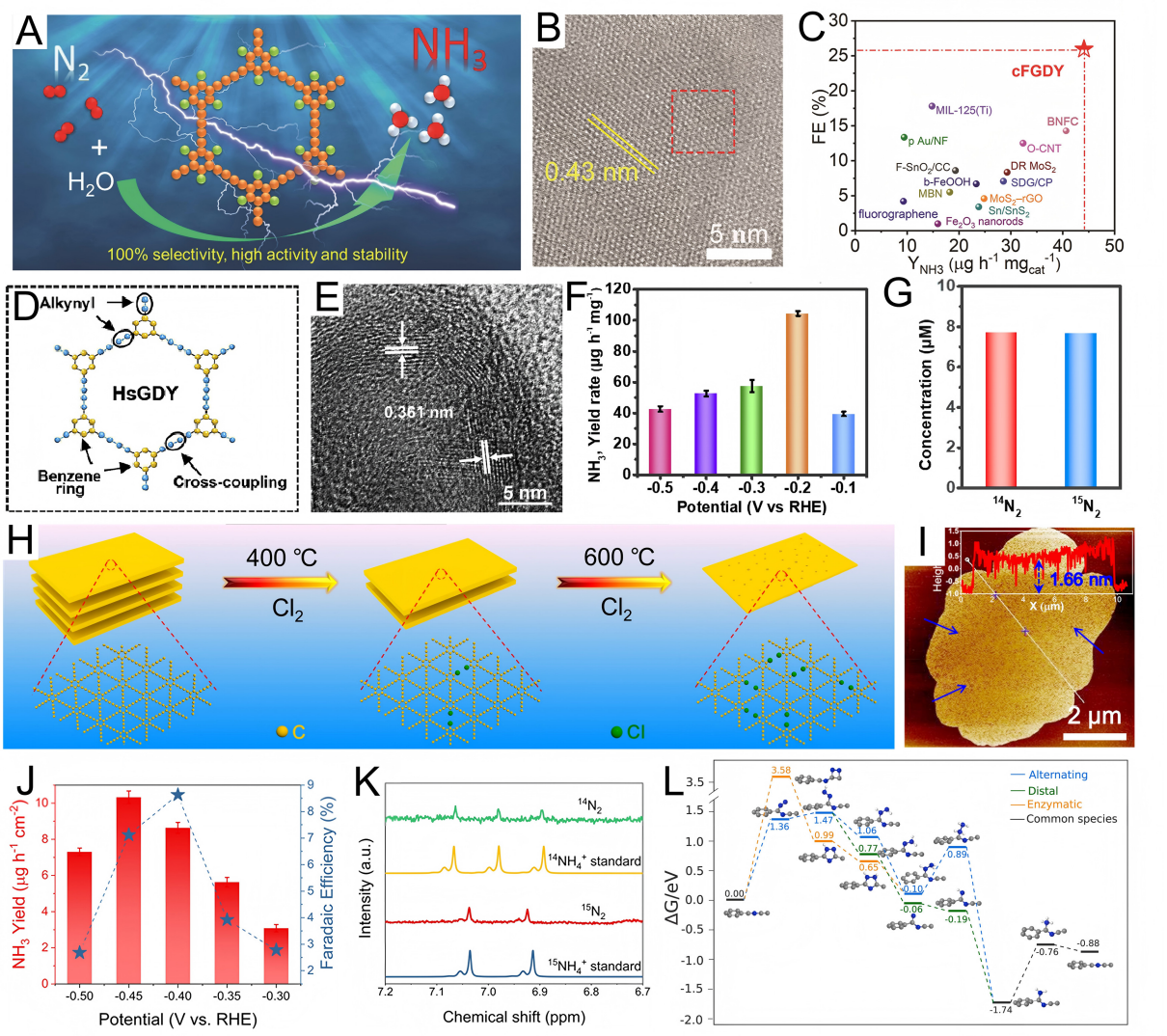

Figure 3. (A) Crystalline cFGDY was prepared for NH_3 synthesis from N_2 and H_2O at ambient conditions, showing 100% selectivity and excellent activity; (B) HRTEM image of cFGDY nanosheets; (C) Y_{NH3} and FEs of cFGDY versus reported metal-free and metal-based catalysts[79]; (A-C) are reprinted with permission from reference[79]. Copyright 2020 The Royal Society of Chemistry; (D) Corresponding schematic illustration of HsGDY; (E) HRTEM image of HsGDY grown on Zn substrate; (F) Calculated NH_3 production rates at different potentials; (G) Concentrations of $(NH_4)_2SO_4$ in the electrolytes when $^{14}N_2$ and $^{15}N_2$ were used as the feed gases[80]; (D-G) are reprinted with permission from reference[80]. Copyright 2020 Elsevier; (H) Illustration of the Cl_2 etching process of GDY; (I) AFM image of Cl-GDY; (J) NH_3 production rates and FE of Cl-GDY; (K) ^1H NMR spectra of $^{15}N_2$- and $^{14}N_2$-fed electrolytes after electrolysis and of commercial $^{14}NH_4Cl$ and $^{15}NH_4Cl$[81]; (H-K) are reprinted with permission from reference[81]. Copyright 2019 American Chemical Society; (L) Free-energy map of NRR over *sp*-N-2 GDY[153]. Reprinted with permission from reference[153]. Copyright 2021 Elsevier B.V. cFGDY: Crystalline fluorinated graphdiyne; HsGDY: hydrogen-substituted graphdiyne; RHE: reversible hydrogen electrode; HRTEM: high resolution transmission electron microscopy.

electron microscopy (HRTEM) analyses [Figure 3A and B]. The high-quality and unique characteristics of cFGDY enable it to act as an efficient metal-free NRR electrocatalyst [Figure 3C], with 100% selectivity toward NH_3 production under room-temperature conditions. The electron-withdrawing fluorine atoms create electron-deficient carbon sites that facilitate N_2 adsorption while suppressing HER[79]. Yang *et al.* presented a scalable protocol in which Zn (instead of traditional Cu) was used as the support for growing planar crystalline HsGDY [Figure 3D and E]. At -0.2 V, the synthesized HsGDY shows outstanding NRR catalytic performance, with an NH_3 yield rate of 103 $\mu g \cdot h^{-1} \cdot mg_{cat.}^{-1}$, which is comparable to or even higher than that of noble metal and state-of-the-art single-atom catalysts [Figure 3F and G][80].

Zou *et al.* introduced a corrosion engineering approach using Cl_2 gas to simultaneously etch and dope bulk GDY [Figure 3H and I][81]. The electronegative Cl atoms form electron-deficient carbon sites that enhance N_2 chemisorption. In performance testing [Figure 3J], Cl-GDY achieves an NH_3 yield rate of 10.7 $\mu g \cdot h^{-1} \cdot cm^{-2}$ and a peak FE of 8.7%. Isotopic labeling with $^{15}N_2$ and $^{14}N_2$ gas feeds [Figure 3K] confirms that the detected ammonia originates directly from dissolved N_2 gas. Supporting these experimental observations, DFT studies have mapped the free energy landscape for NRR on various heteroatom-doped GDY systems. Wang *et al.* investigated four different N-doped GDY models and found that *sp*-N-2-substituted GDY exhibits the highest activity, with nitrogen doping at *sp*-hybridized acetylenic sites reducing the energy barrier for the potential-limiting step ($N_2(g) \rightarrow$HN-N) to -0.99 V through a hybrid pathway [Figure 3L][153]. Computational investigations further validate the efficacy of heteroatom doping in metal-free graphdiyne, as evidenced by DFT calculations on oxygen-doped GDY (O-doped GDY)[156], single-boron-substituted GDY at acetylenic sites (B(S3)@GDY), and dual-boron-doped GDY frameworks (GDY-2B(S2 S2'))[157], which collectively demonstrate enhanced N_2 activation and reduced reaction barriers.

The above results are summarized in Figure 3. The conjugated backbone of GDY, upon heteroatom doping or polarization modulation, forms electrondeficient carbon active centers, which strengthen dinitrogen activation and suppress side reactions while eliminating metal dependence, thereby achieving highly selective and efficient nitrogen-to-ammonia conversion.

Heterostructured GDY catalysts for the NRR

The abundant *sp*/sp^2-hybridized carbon, delocalized π-electrons, and regular acetylenic pores of GDY render it an ideal substrate for constructing heterostructured electrocatalysts. When combined with transition metal nitrides, oxides, borides, or QDs, GDY modulates interfacial charge redistribution and tunes the electronic states of the active sites. This optimizes light absorption and electrical conductivity while simultaneously restraining the competing HER and facilitating N≡N bond cleavage for the NRR[158,159].

Defect and interface engineering of GDY-based heterostructured electrocatalysts has shown great potential for enhancing ambient nitrogen reduction. Fang *et al.* designed an Fe-vacancy-rich Fe_3O_4/graphdiyne heterostructure (IVR-FO/GDY) through coprecipitation and a cross-coupling sequence [Figure 4A and B]. Owing to the synergistic interaction between GDY and Fe_3O_4, many Fe vacancies were introduced in IVR-FO/GDY, and the valence state of Fe was precisely regulated, thus improving the catalytic performance[82]. In neutral 0.1 M Na_2SO_4, IVR-FO/GDY achieves a peak NH_3 yield (Y_{NH_3}) of 127.92 ± 9.11 $\mu g \cdot h^{-1} \cdot mg_{cat.}^{-1}$ and a FE of 59.48% ± 2.57% at 0.255 V *vs.* RHE [Figure 4C], vastly outperforming pristine Fe_3O_4 and bare GDY. Interfacial regulation can also effectively mitigate competitive HER. Fang *et al.* constructed a self-standing 3D GDY/Co_2N composite by nitriding cobalt layered double hydroxide (CoLDH) nanowires, followed by *in situ* growth of GDY films [Figure 4D]. Transmission electron microscope (TEM) imaging [Figure 4E] illustrates the core-shell nanowire morphology when an ultrathin GDY coats the Co_2N core. The rich acetylenic bonds in GDY draw electrons from Co_2N, creating electron-deficient Co sites that favor N_2 adsorption while increasing the kinetic barrier for H chemisorption. In neutral media, GDY/Co_2N maintains stable performance across multiple cycles, delivering a high NH_3 yield rate and FE [Figure 4F][83].

Photocatalytic nitrogen fixation represents another promising direction for GDY heterostructures, wherein GDY acts as an electron acceptor to accelerate photogenerated carrier separation and lower activation barriers[162,163]. Liu *et al.* reported porous GDY loaded with cobalt oxide quantum dots (GDY@CoO_xQD) [Figure 4G][160]. HRTEM [Figure 4H] shows ultrasmall CoO_xQDs (~3.75 nm) uniformly anchored across the porous GDY nanosheets. Under light irradiation in water, the mixed Co^{2+}/Co^{3+} valence states and surface plasmon resonance (SPR)-like behavior drive directional electron flow to GDY. In aqueous testing [Figure 4I], GDY@CoO_xQD yields an extraordinary average NH_3 formation rate of 19,583 $\mu mol_{NH_3} \cdot g_{cat}^{-1} \cdot h^{-1}$, whereas

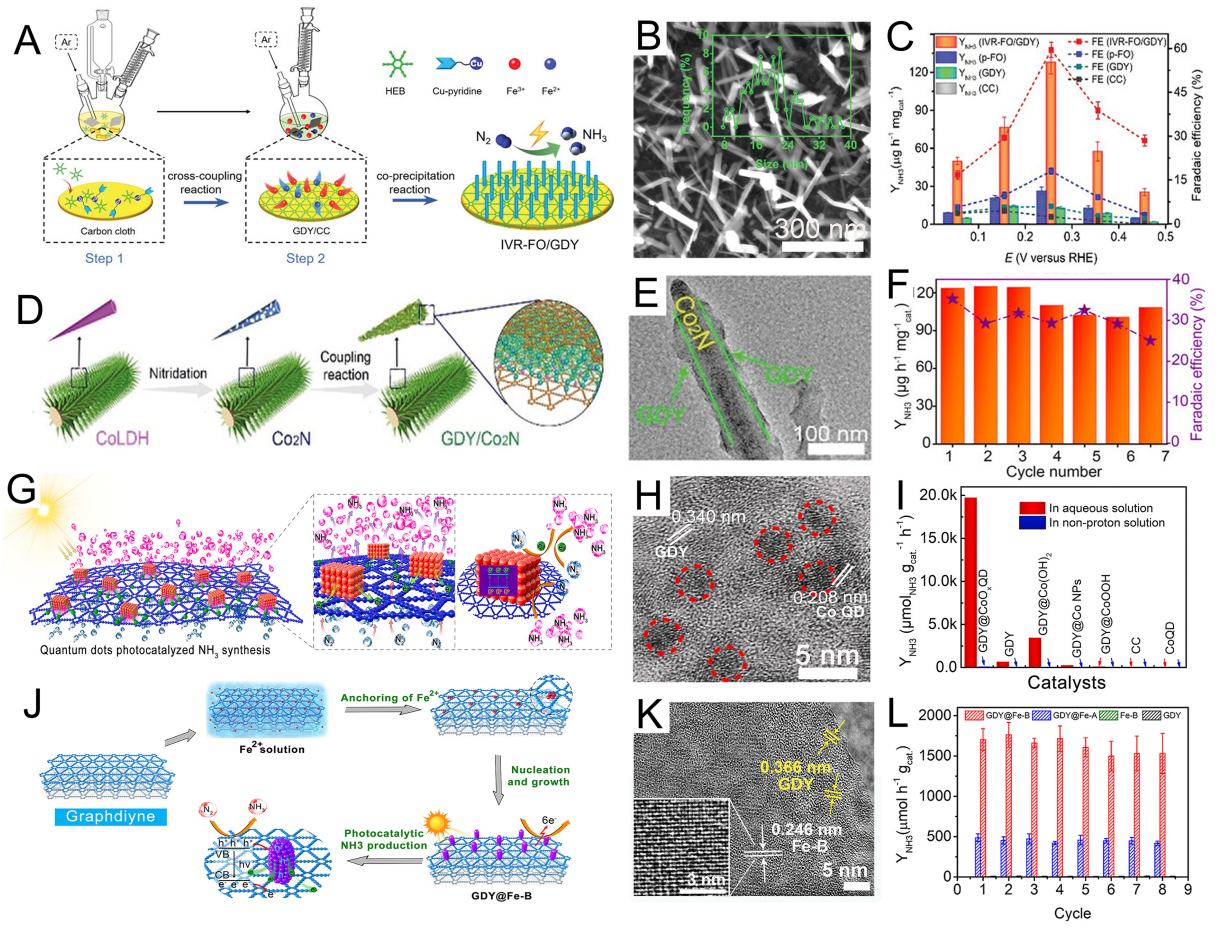

Figure 4. (A) Schematic illustration of IVR-FO/GDY preparation; (B) SEM of IVR-FO/GDY; (C) Y_{NH3} and FEs of the samples at different potentials in N_2-saturated 0.1 M Na_2SO_4 (error bars represent the standard deviation)[82]; (A-C) are reprinted with permission from reference[82]. Reproduced under the CC BY 4.0 license; (D) Synthesis of self-supported GDY/Co_2N; (E) TEM image of GDY/Co_2N. NRR performance of GDY/Co_2N in (F) neutral media[83]; (D-F) are reprinted with permission from reference[83]. Copyright 2020 Wiley-VCH Verlag GmbH & Co. KGaA, Weinheim; (G) Schematic diagram of the ammonia production process on porous GDY@CoO_xQD; (H) HRTEM images of porous GDY@CoO_xQD nanosheets; (I) Y_{NH3} of the samples in different electrolytes[160]; (G-I) are reprinted with permission from reference[160]. Copyright 2021 Elsevier; (J) Preparation and reaction route for GDY@Fe-B; (K) HRTEM images of GDY@Fe-B; (L) Y_{NH3} obtained after the stability test[161]; (J-L) are reprinted with permission from reference[161]. Copyright 2020 Wiley-VCH GmbH. IVR-FO/GDY: Iron vacancy (VFe)-rich ferroferric oxide on GDY; HEB: hexaethynylbenzene; CC: carbon cloth; FE: Faradaic efficiency; RHE: reversible hydrogen electrode; SEM: scanning electron microscope; NRR: nitrogen reduction reaction; TEM: transmission electron microscope; HRTEM: high resolution transmission electron microscopy.

nonprotonic solvents or control catalysts yield negligible amounts of ammonia, confirming that water is the proton donor[160]. Fang *et al.* developed a Janus magnetite/GDY nanorod heterostructure (GDY@Fe-B). Rod-shaped GDY@Fe_3O_4 (GDY@Fe-B) was controllably synthesized [Figure 4J]. HRTEM [Figure 4K] displays distinct lattice fringes of GDY (0.365 nm) and Fe-B (0.246 nm), with nanorod lengths distributed approximately 15-25 nm (inset). Under light and magnetic field assistance, the Janus interface exhibits enhanced charge separation. Consequently, compared with the GDY, Fe-B, and non-Janus GDY@Fe-A controls, GDY@Fe-B maintains superior photocatalytic stability over 8 cycles [Figure 4L], achieving markedly higher NH_3 yields. This study fully exploits the structural and intrinsic properties of GDY and pioneers a new avenue for photocatalysis[161]. In a single-molybdenum-atom-decorated hydrogen-substituted graphdiyne photocathode system (Mo_1/HsGDY@Cu_2O)[84], Cu_2O generates photogenerated electrons, while the alkynyl-rich network of HsGDY serves not only as a charge transport channel but also efficiently dissociates water to supply active H·. Concurrently, the adjacent Mo1 single-atom sites function as robust centers for N_2 adsorption and activation, markedly lowering the hydrogenation activation barrier. Under

standard simulated sunlight irradiation [Air mass (AM) 1.5G, 100 $mW \cdot cm^{-2}$, 0 V *vs.* RHE], this system delivers an NH_3 yield rate of 15.8 $\mu g \cdot h^{-1} \cdot cm^{-2}$ with an FE of 42.8%. Remarkably, under 10-sun concentrated solar illumination, the NH_3 yield rate surges to a record 78.9 $\mu g \cdot h^{-1} \cdot cm^{-2}$ alongside a FE of 38.9%, retaining 86% of its initial catalytic activity after continuous operation for 240 h. This breakthrough further substantiates the universal utility of GDY-based materials in stabilizing single-atom sites, mediating *in situ* active hydrogen supply, and modulating interfacial charge dynamics.

GDY-based catalysts exhibit exceptional catalytic activity in photocatalytic nitrogen fixation, primarily due to GDY's unique framework structure and strong electronic coupling with active centers[164,165]. First, the intrinsic uniform microporous structure and the enyne-rich backbone (sp/sp^2-hybridized carbon) endow GDY with a highly heterogeneous surface charge distribution and strong reducibility, providing ideal anchoring sites for active metal species and effectively preventing their aggregation and deactivation during the reaction. Second, pronounced interfacial charge transfer and orbital hybridization occur between GDY and the supported metals, which, under light irradiation, accelerate the dynamic valence-state transitions of the metals and facilitate efficient electron transfer to the π^* antibonding orbitals of adsorbed N_2, thereby substantially reducing the N≡N bond strength and decreasing the protonation energy barrier. Moreover, GDY not only significantly enhances the localized SPR effect but also serves as a fast electron-transport channel, effectively suppressing photogenerated charge-carrier recombination and improving the apparent quantum efficiency.

GDY-based Catalysts for NtRR

Electrochemical NtRR is thermodynamically more favorable than NRR, as the nitrogen-oxygen bond energy (204 $kJ \cdot mol^{-1}$) is substantially lower than that of the nitrogen-nitrogen triple bond (941 $kJ \cdot mol^{-1}$)[166,167]. Beyond this thermodynamic advantage, nitrate is one of the most widespread pollutants in water bodies, presenting severe risks to human health and interfering with the natural nitrogen cycle in ecosystems[168]. Driven by renewable electricity, the conversion of nitrate into value-added ammonia under ambient conditions can simultaneously achieve two objectives: pollutant degradation and ammonia generation. However, electrochemical nitrate-to-ammonia conversion involves a complex multielectron transfer route, requiring nine protons and eight electrons per nitrate ion ($NO_3^- + 9H^+ + 8e^- \rightarrow NH_3 + 3H_2O$)[169,170]. The existence of various reaction intermediates, including NO_2^-, NO, N_2O, and NH_2OH, further complicates the mechanistic understanding of interfacial processes on the electrode surface, presenting a major challenge in attaining high selectivity for ammonia production in NtRR[3]. In recent years, GDY-based catalysts have demonstrated notable advantages and achieved significant progress in the field of nitrogen fixation, exhibiting superior FE, ammonia yield, and stability relative to other carbon-based materials.

GDY-based metal atom catalysts for NtRR

Integrating low-dimensional metals, from QDs[171] and subnanometer clusters[172] to single-atom sites[173], onto GDY offers an effective platform for the electrochemical reduction of nitrogenous species. Catalytic design and interface engineering play a central role in driving nitrate electroreduction[167]. A prime example is the Cu/Cu_xO/GDY catalyst engineered by Feng *et al.* [Figure 5A][85]. The proposed reaction scheme exploits spatial catalytic coupling, in which the Cu/Cu_xO interface promotes the initial conversion of NO_3^- to NO_2^-, after which the surrounding GDY matrix captures the released NO_2^- to drive subsequent hydrogenation to NH_3. HRTEM [Figure 5B] reveals intimate phase boundaries between the $Cu_xO(110)$ (0.286 nm) and Cu(111) (0.209 nm) domains on GDY. This cooperative pathway yields an NH_3 production rate (Y_{NH_3}) exceeding 34,000 $\mu g \cdot h^{-1} \cdot mg_{cat}^{-1}$ and a FE close to 100% at -0.9 V *vs.* RHE [Figure 5C]. Extending this concept to bimetallic QDs, Wu *et al.* synthesized amorphous/crystalline $PtCu_x$ QDs on GDY ($PtCu_x$/GDY) via microwave-assisted anchoring and thermal annealing [Figure 5D]. Characterization revealed "incomplete charge transfer" across the QD-GDY heterojunction interface [Figure 5E], where localized electronic

redistribution stabilized mixed valence states (Pt^0/Pt^{2+} and Cu^0/Cu^{2+}) to prevent intermediate overbinding. Consequently, $PtCu_x$/GDY achieves a Y_{NH_3} of 345.3 ± 38.9 μmol·h^{-1}·cm^{-2} and an FE of 96.5 ± 5.1% at -0.5 V *vs.* RHE [Figure 5F][86]. Ligand-mediated electronic tuning allows precise control over the local coordination sphere. Wang *et al.* introduced fluorine modifications to single Pd atoms on GDY (Pd/GDY-F). The chemical structure [Figure 5G] shows how electron-withdrawing F atoms on the aromatic ring alter the conjugated backbone, increasing the oxidation state of the central Pd site. Aberration-corrected HAADF-STEM [Figure 5H] verifies the atomic dispersion of Pd. For NtRR, Pd/GDY-F delivers an NH_3 yield exceeding 5,000 μg·h^{-1}·mg_{Pd}^{-1} at -1.1 V *vs.* RHE [Figure 5I], significantly outperforming the other catalysts [Figure 5J]. This is because F-induced electron withdrawal increases the activation barrier for H* formation, mitigating the competitive HER[87].

Zero-valent metal atom arrays offer an alternative approach to single-site catalysis. Zheng *et al.* constructed a zero-valent copper single-atom array on GDY (Cu^0/GDYNA) through *in situ* coordination and self-reduction of Cu^{2+} on 3D GDY nanoarrays [Figure 5K and L]. HAADF-STEM [Figure 5M] confirms the presence of dense, monodisperse Cu^0 single atoms anchored within acetylenic cavities. At -2.0 V *vs.* SCE, Cu^0/GDYNA delivers a maximum FE of 81.25% [Figure 5N]. The synthesis and application of Cu^0/GDYNA catalysts open up a new field of GDY-based ACs[88]. Complementing these experimental efforts, theoretical calculations provide mechanistic insight into overcoming linear scaling relationships across single-atom, dual-atom, and multi-atom configurations. DFT modeling of single-atom Os/GDY[174] indicated that it is an effective NtRR catalyst with a limiting potential as low as -0.37 V and pronounced suppression of competing reactions. In dual-atom configurations such as TiCu@GDY, calculations demonstrate a site-coupling effect: electrophilic Ti promotes nitrate activation, whereas adjacent Cu lowers the water dissociation barrier (ΔG_{act} = 0.64 eV) to supply H, yielding a theoretical limiting potential of -0.20 V[175]. Extending this to multicenter clusters, N-doped carbon-supported trimers (Co_2Ni, Co_2Cu, and Fe_2Ni) show a theoretical limiting potential of 0.00 V *vs.* RHE without a distinct potential-determining step in NtRR[176]. Moreover, Mn_3-GDY clusters induce spin polarization, which triggers a pathway separation mechanism ($NO_3H \rightarrow NO_2^* + OH^*$), reducing the limiting potential to 0.23 V and lowering the NH_3 desorption barrier to 0.18 eV[177]. These studies demonstrate that integrating the *sp*-hybridized carbon network of GDY with low-dimensional metal centers effectively optimizes intermediate adsorption, reduces rate-limiting energy barriers, and suppresses competing HER during electrocatalytic nitrogenous transformations.

GDY-based heterojunction catalysts for NtRR

Beyond single-component metal/metal compound catalysts, GDY-based heterojunctions offer a particularly powerful platform for NtRR by exploiting synergistic interfacial effects. The *sp*- and sp^2-hybridized carbon network and alkynyl bonds of GDY modulate inorganic phase growth while inducing local strain and defects. This creates efficient interfacial charge-transport pathways that optimize intermediate adsorption and suppress the HER[89,90,92].

Zhang *et al.* synthesized a Cu_3N/GDY catalyst with a nitride/GDY interface that operates via an *in situ* vacancy generation mechanism [Figure 6A and B][89]. Under an applied potential, GDY accelerates water dissociation to generate reactive hydrogen radicals, which attack the lattice nitrogen of Cu_3N to form nitrogen vacancies. The resulting nitrogen-vacancy sites and GDY matrix modulate the local electron density of adjacent Cu atoms, thus promoting NO_3^- adsorption and hydrogenation, achieving an ammonia yield rate (Y_{NH_3}) of 35,280 μg·h^{-1}·$mg_{cat.}^{-1}$ and a FE of 98.1% at -0.9 V *vs.* RHE [Figure 6C and D]. Figure 6E and F show the synthesis of the Cu_2O/GDY composite using electron beam irradiation. Optimizing the Cu loading prevented nanoparticle aggregation while maintaining a high active-site density, enabling the catalyst to achieve an FE of 94% and an NH_3 yield of 26,997 μg·h^{-1}·$mg_{cat.}^{-1}$ at -1.7 V *vs.* Hg/HgO [Figure 6G and H][90]. Furthermore, Cu_xO grown on pyridine-nitrogen-dominated nitrogen-doped GDY[91] utilizes the synergistic effect of pyridine nitrogen and Cu_xO to accelerate H* formation, achieving an 89% FE in a fluidized bed.

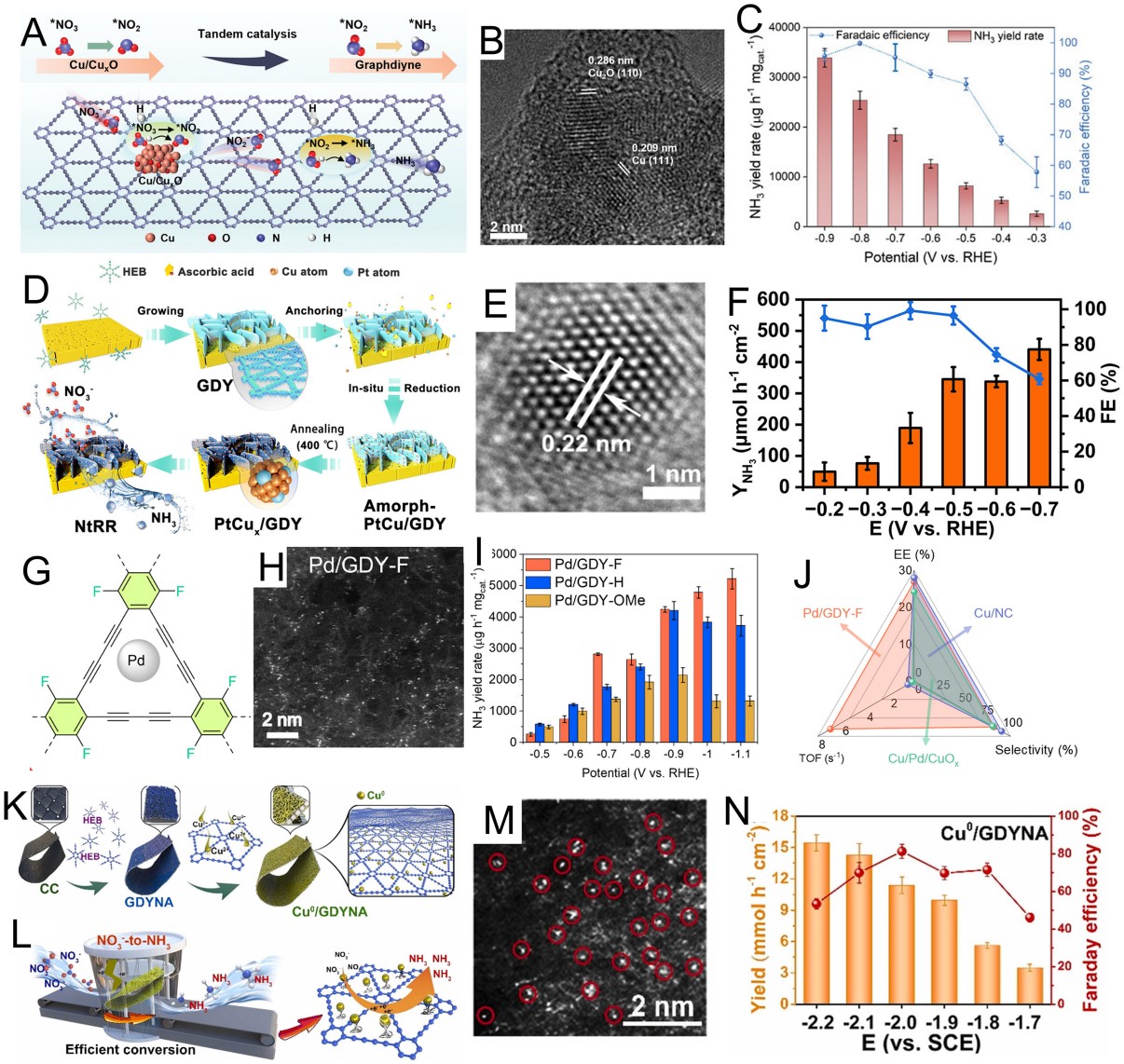

Figure 5. (A) Proposed reaction scheme for the NtRR on Cu/Cu$_x$O/GDY; (B) HRTEM image of Cu/Cu$_x$O/GDY; (C) Y_{NH3} and FEs of Cu/Cu$_x$O/GDY at selected potentials[85];(A-C) are reprinted with permission from reference[85]. Copyright 2024 Wiley-VCH GmbH; (D) Schematic illustration of PtCu$_x$/GDY synthesis; (E) HRTEM image of PtCu$_x$/GDY; (F) PtCu$_x$/GDY Y_{NH3} and FE at varied potentials[86]; (D-F) are reprinted with permission from reference[86]. Copyright 2024 American Chemical Society; (G) Chemical structure of Pd/GDY-F; (H) AC-HAADF-STEM image of Pd/GDY-F; (I) Rate of NH_3 production in the NtRR for Pd/GDY-R (R = F, H, OMe); (J) Comparison of catalytic performance between Pd/GDY-F and other catalysts[87]; (G-J) are reproduced without modification from reference[87]. Reproduced under a CC BY-NC-ND 4.0 license; (K) Schematic of the synthesis route and (L) the NtRR process of Cu^0/GDYNA; (M) HAADF-STEM image of Cu^0/GDYNA; (N) Y_{NH3} and FEs of Cu^0/GDYNA catalysts at different potentials[88]; (K-N) are reprinted with permission from reference[88]. Copyright 2022 Elsevier. GDY: Graphdiyne; NtRR: nitrate reduction reaction; RHE: reversible hydrogen electrode; TOF: turnover frequency; EE: energy efficiency; CC: carbon cloth; GDYNN: GDY nanosheets; SCE: saturated calomel electrode; HRTEM: high resolution transmission electron microscopy; FE: Faradaic efficiency; AC-HAADF-STEM: aberration-corrected high-angle annular dark-field scanning transmission electron microscopy.

Introducing planar defects into one-dimensional structures can accelerate reaction kinetics. Luan *et al.* synthesized grain boundary-rich one-dimensional $CuCo_2O_x$/GDY nanowires, where the coordination of *sp* carbon with metal sites induces high-angle grain boundaries and localized strain in the nanowires [Figure 6I and J]. When used for NtRR, $CuCo_2O_x$/GDY achieved ~100% FE and a yield rate of 3,332 μg·cm^{-2}·h^{-1} in 1.0 M

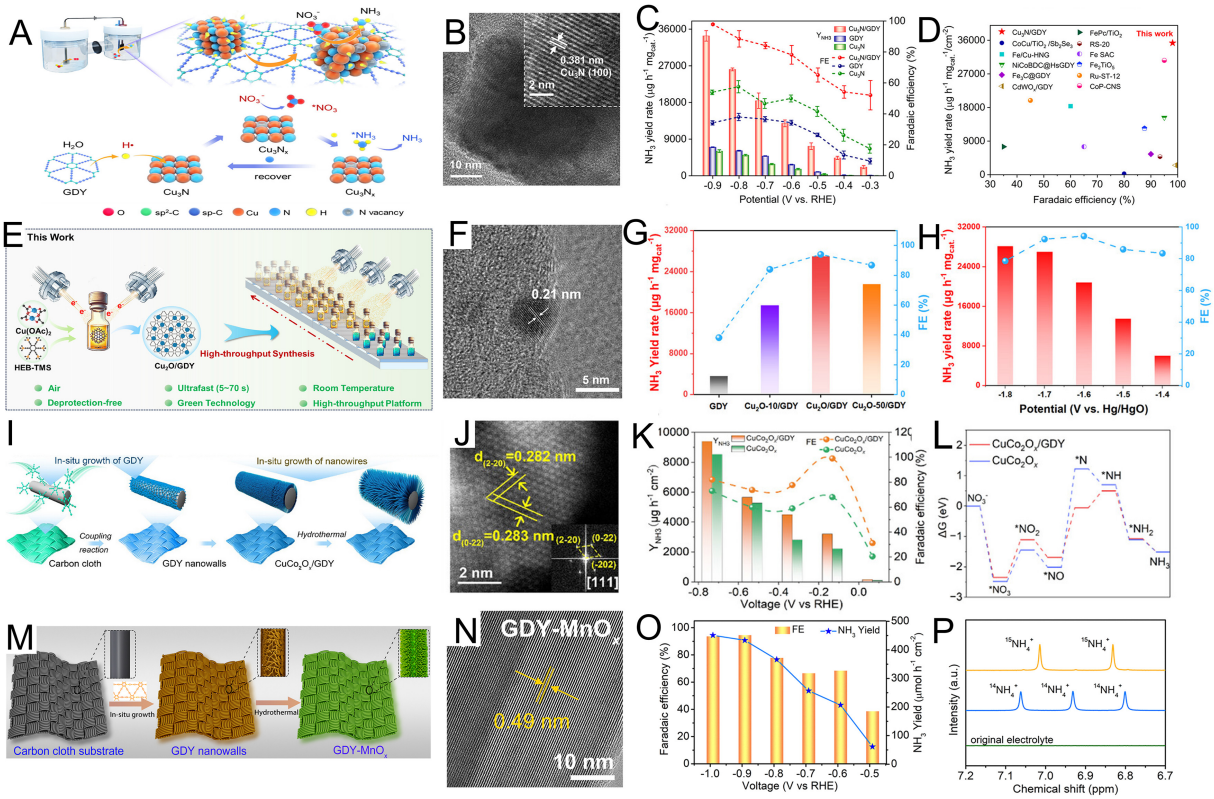

Figure 6. (A) Design and operation of the Cu_3N/GDY catalyst for NtRR; (B) HRTEM image of the Cu_3N/GDY catalyst; (C) Y_{NH3} and FEs of the Cu_3N/GDY and the other samples at different potentials; (D) Comparison of Cu_3N/GDY with recently reported catalysts. (The nitrate concentrations of these reports are equal to or exceed 0.1 M)[89]; (A-D) are reprinted with permission from reference[89]. Copyright 2024 American Chemical Society; (E) Electron beam irradiation synthesis; (F) HRTEM image of Cu_2O/GDY NtRR performance and mechanistic analysis; (G) NH_3 yield rates and FEs at different Cu loadings and (H) for Cu_2O/GDY at different potentials[90]; (E-H) are reprinted with permission from reference[90]. Copyright 2025 Wiley-VCH GmbH; (I) Synthesis routes of $CuCo_2Ox$/GDY; (J) HRTEM image showing the lattice fringes and high-angle grain boundaries of $CuCo_2O_x$/GDY; (K) Comparison of Y_{NH3} and FEs of $CuCo_2Ox$ and $CuCo_2Ox$/GDY; (L) Free energy diagram for $CuCo_2Ox$/GDY and $CuCo_2Ox$[92]; (I-L) are reprinted with permission from reference[92]. Copyright 2025 Wiley-VCH GmbH; (M) Synthesis routes to GDY-MnO_x; (N) HRTEM image of GDY-MnO_x; (O) FEs and Y_{NH3} of GDY-MnO_x at different potentials; (P) ^1H NMR of electrolytes following reduction of $^{15}NO_3^-$ and $^{14}NO_3^-$[95]; (M-P) are reprinted with permission from reference[95]. Copyright 2023 The Royal Society of Chemistry. GDY: Graphdiyne; RHE: reversible hydrogen electrode; HEB-TMS: Hexakis-[(trimethylsilyl)ethynyl]benzene; FE: Faradaic efficiency; NtRR: nitrate reduction reaction; HRTEM: high resolution transmission electron microscopy.

KOH + 0.1 M NO_3^- aqueous solution at a potential of -0.132 V *vs.* RHE [Figure 6K]. Mechanistic analysis shows that interfacial defects on $CuCo_2O_x$/GDY could effectively reduce the energy barrier of the deoxygenation step ($*NO_2 \rightarrow *NO \rightarrow *N$) from 3.23 to 1.63 eV [Figure 6L][92]. Similarly, Co_3O_4/GDY nanowires[93] achieved 92.45% FE by utilizing *sp*-C–Co bonds and incomplete charge transfer to facilitate continuous electron transfer at -1.05 V *vs.* RHE. GDY heterojunctions can also be extended to manganese-based systems [GDY-MnO_x; Figure 6M]. HRTEM [Figure 6N] confirmed that the interplanar spacing of MnO_x was 0.49 nm. The charge transfer from *sp* carbon to Mn reduced the average oxidation state of Mn from 3.74 to 3.52, increasing the proportion of Mn^{3+} sites. GDY-MnO_x achieved 95.4% FE and 463.4 μmol·h^{-1}·cm^{-2} at -0.891 V *vs.* RHE [Figure 6O]. Isotope labeling experiments [Figure 6P] confirmed that the ammonia was entirely derived from nitrate reduction[95].

Leveraging the inherent properties of GDY, diverse GDY-based heterojunction catalysts (e.g., h-FeCoNiPBA@GDY and Fe_3C@GDY) have been rationally fabricated and deployed for electrocatalytic nitrogen fixation toward ammonia synthesis[99]. The integration of GDY with metal coordination nanostructures offers a complementary strategy for constructing high-performance NtRR catalysts. The

well-defined porous architecture and abundant coordination sites of metal-organic coordination compounds, when coupled with GDY's exceptional conductivity and electronic tunability, create interfaces that enhance nitrate-to-ammonia conversion. Zhao *et al.* developed a hybrid architecture by growing a conformal GDY layer directly on zeolitic imidazolate framework nanocubes (ZIFNC@GDY)[96]. As shown in Figure 7A-C, Co^{2+} and 2-methylimidazole self-assemble into ZIF-67 nanocubes (ZIFNC) nanocubes, which then serve as a template to catalyze the growth of a GDY shell. ZIFNC and GDY function as the electron acceptor and donor, respectively, linked through covalent *sp*-C–Co and *sp*-C–N bonds to establish an efficient charge-transfer channel. This configuration increases the electron density on the GDY surface and enhances nitrate electroreduction activity. High-magnification TEM images [Figure 7D and E] verify the well-defined architecture, showing a crystalline ZIFNC core encapsulated by a uniform GDY layer. The high-resolution image reveals 0.251 nm lattice fringes for the ZIFNC core and a 0.335 nm interlayer spacing for the outer GDY layer [Figure 7E]. In neutral aqueous media, ZIFNC@GDY outperforms bare ZIFNC across the entire potential range [Figure 7F and G], reaching a peak FE_{NH_3} of 98.51% ± 0.75% with an ammonia yield rate of 0.40 ± 0.02 mmol·h^{-1}·cm^{-2} at -1.4 V *vs.* SCE (-0.745 V *vs.* RHE).

To address intermediate adsorption mismatches during nitrate reduction, Wang *et al.* designed a dual-interface tandem catalyst (NiBDC@HsGDY@Cu) by linking ultrathin Ni-BDC MOF nanosheets with HsGDY carrying Cu single atoms and clusters[97]. As illustrated in Figure 7H, ultrathin NiBDC nanosheets are conformally wrapped with a thin HsGDY layer via the Glaser coupling of 1,3,5-triethynylbenzene, followed by the electrodeposition of Cu single atoms/clusters onto the HsGDY framework. Within this 0-3.6 nm interface, HsGDY acts as a conductive bridge. Unsaturated Ni^{2+} sites promote H_2O cleavage to generate active *H species that spill over via HsGDY to Cu sites, while NO_2^- released from Cu sites diffuses to Ni^{2+} sites to complete the cascade conversion of NO_3^- to NH_3. In 1 M KOH + 0.1 M KNO_3, NiBDC@HsGDY@Cu retained high selectivity (FE_{NH_3} > 90%) across a broad window from -0.01 to -0.51 V *vs.* RHE [Figure 7I], markedly exceeding the performance of individual HsGDY@Cu and NiBDC. At a low overpotential of -0.11 V *vs.* RHE, the catalyst achieves an FE_{NH_3} of 95.5% and a Y_{NH_3} of 0.321 mmol·h^{-1}·cm^{-2}.

For bimetallic coordination systems, Ma *et al.* synthesized a self-supported NiCoBDC@HsGDY nanowire array on carbon paper[98]. As depicted in Figure 7J, NiCo carbonate hydroxide (NiCoHC) nanowires serve as initial templates. A protective HsGDY layer is polymerized on their surface via Glaser coupling, followed by a solvothermal anion-exchange reaction with 1,4-benzenedicarboxylic acid (BDC). The outer HsGDY shell acts as a physical cage that confines the *in situ* transformation, yielding well-aligned NiCoBDC@HsGDY core-shell nanowires, as shown by the SEM image in Figure 7K. Electronic coupling between Ni^{2+} and Co^{2+} drives partial charge transfer from Ni^{2+} to coordinatively unsaturated Co^{2+} sites through bridging O_2^- ligands, simultaneously optimizing NO_3^- deoxygenation at Co^{2+} and H_2O activation at Ni^{2+}. Consequently, NiCoBDC@HsGDY outperforms its monometallic counterparts (CoBDC@HsGDY and NiBDC@HsGDY) as well as pristine NiCoBDC in terms of geometric yield [Figure 7L], delivering a Y_{NH_3} of 0.56 mmol·h^{-1}·cm^{-2} with an FE_{NH_3} of 99.1% at -0.34 V *vs.* RHE in alkaline media.

These breakthroughs underscore that graphdiyne is a uniquely powerful and versatile platform for engineering advanced NtRR electrocatalysts. By integrating various active domains onto the *sp*/sp^2 carbon matrix of GDY, researchers can trigger synergistic phenomena such as incomplete charge transfer, interfacial strain, and tuned coordination environments. These modifications fundamentally bypass the scaling limitations of single-site catalysts, lower energy barriers for rate-limiting deoxygenation and hydrogenation steps, and effectively eliminate the competitive HER. As a result, GDY-based heterostructured architectures provide a clear roadmap for achieving ultrahigh-rate, selective, and durable nitrate-to-ammonia electrosynthesis, bridging the gap between fundamental catalyst design and practical industrial water treatment/energy conversion applications.

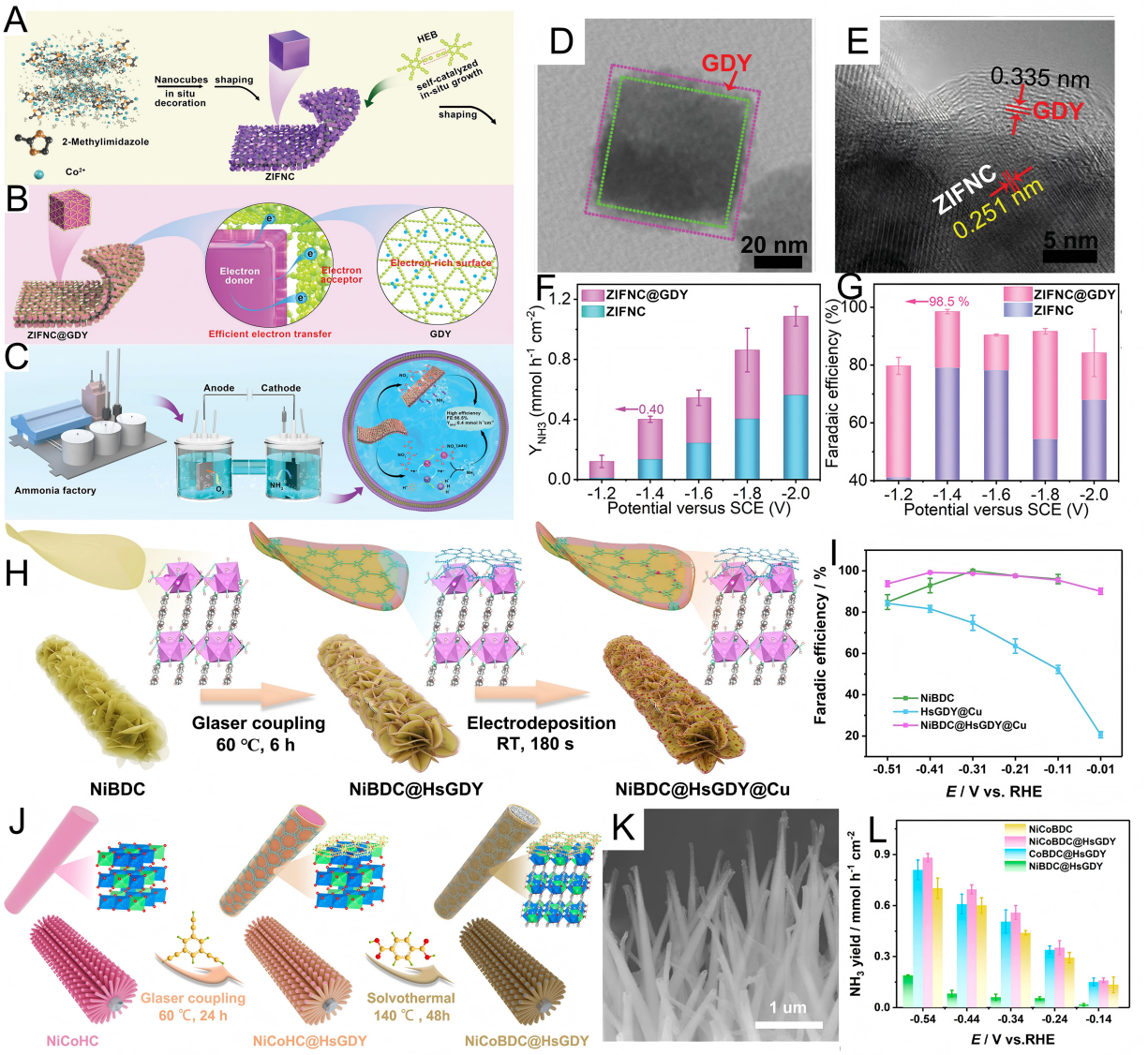

Figure 7. Schemes for (A) ZIFNC preparation, (B) ZIFNC@GDY, and (C) their application to NH_3 production; (D and E) HRTEM images of ZIFNC@GDY; (F) Y_{NH3} at different potentials of ZIFNC@GDY and ZIFNC; (G) FEs at different potentials of ZIFNC@GDY and ZIFNC[96]; (A-G) are reprinted with permission from reference[96]. Copyright 2022 Wiley-VCH GmbH; (H) Schematic for integrating Ni-MOF ultrathin nanosheets with few-layer HsGDY-supported Cu single atoms and clusters; (I) Potential-dependent FE_{NH3} of NiBDC, HsGDY@Cu and NiBDC@HsGDY@Cu[97]; (H and I) are reprinted with permission from reference[97]. Copyright 2024 Wiley-VCH GmbH; (J) Scheme for fabrication of NiCoBDC@HsGDY nanowire array; (K) SEM image of the NiCoBDC@HsGDY nanoarray; (L) Potential-dependent Y_{NH3} normalized by geometric area over NiCoBDC, NiCoBDC@HsGDY, CoBDC@HsGDY, and NiBDC@HsGDY[98]; (J-L) are reprinted with permission from reference[98]. Copyright 2023 American Chemical Society. GDY: Graphdiyne; ZIFNC: ZIF-67 nanocubes; SCE: saturated calomel electrode; NiBDC: Ni-benzenedicarboxylic acid; RT: room temperature; RHE: reversible hydrogen electrode.

CONCLUSION AND OUTLOOK

Graphdiyne has been demonstrated to be an ideal active carbon platform for selective and efficient nitrogen fixation. Its *sp*/*sp*^{2}-cohybridized framework, characterized by intrinsic electronic heterogeneity, fundamentally distinguishes GDY from all other carbon allotropes and provides interconnected advantages for catalyst design, such as electronic modulation through noninteger charge transfer, spatial confinement within intrinsic pores, and interfacial synergy in heterostructures, thereby addressing the core challenges of electrochemical ammonia synthesis. In NRR, GDY-based catalysts have achieved unprecedented activities and selectivities by stabilizing unconventional zero-valent metal states, optimizing *d*-band centers for N_2

activation, and effectively suppressing the competing HER. In NtRR, near-unity Faradaic efficiencies and record-high ammonia yields are realized through nitrate enrichment, decoupling of deoxygenation and hydrogenation steps on distinct active sites, and stabilization of key intermediates. We further emphasize that the reliability and reproducibility of NRR performance data critically depend on the rigorous exclusion of exogenous nitrogen contaminants. The adoption of standardized testing protocols[34], including electrolyte purification, high-purity N_2 feedstock, inert-atmosphere control experiments, and routine isotopic labeling ($^{15}N_2/^{14}N_2$), is indispensable for establishing reliable performance benchmarks across laboratories. Such standardized procedures are essential for expediting the discovery of genuinely promising catalysts. This methodological rigor, combined with the development of reference GDY materials, will provide a solid foundation for the rational design of next-generation NRR catalysts and facilitate their translation toward practical ammonia electrosynthesis.

Despite these impressive achievements, the translation of GDY-based catalysts from fundamental breakthroughs to practical, industrial-scale ammonia production confronts substantial challenges, such as scalable synthesis of high-quality GDY, long-term stability under complex industrial conditions, and the lack of operando verification for the dynamic evolution of active sites. Notably, while most research focuses on ambient electrochemical routes, industrial ammonia production remains dominated by the high-temperature, high-pressure Haber-Bosch process. Bridging this gap requires addressing the thermal stability of GDY-based catalysts under harsh reducing conditions, the transferability of mechanistic insights from electrochemical to thermal systems, and the scalability of GDY synthesis for industrial fixed-bed or fluidized-bed reactors. Moreover, scaling GDY synthesis from laboratory to kilogram quantities poses additional engineering challenges distinct from electrochemical cell assembly. Addressing these challenges will require interdisciplinary efforts that combine thermal catalysis with the unique electronic properties of GDY, potentially leading to hybrid thermal-electrocatalytic systems or GDY-based catalysts for photothermal or plasma-assisted ammonia synthesis.

Looking forward, three strategic directions are particularly promising. First, scalable and cost-effective synthesis must transition from laboratory-scale methods to continuous-flow routes using earth-abundant catalysts, preserving crystallinity and electronic properties. Second, deeper mechanistic understanding of GDY as an active support is urgently needed; the dynamic evolution of the GDY framework, including structural rearrangements, metal migration, and alkyne bond participation, remains poorly understood. Advanced operando characterization coupled with machine-learning-accelerated simulations will be essential to establish true structure-activity-selectivity correlations. Third, photocatalytic nitrogen fixation represents an underexplored frontier; GDY's tunable bandgap and charge-carrier mobility make it ideal for light-driven ammonia synthesis. Integration with plasmonic nanoparticles, semiconductor heterojunctions, or photosensitizers could enable solar-to-chemical conversion, offering a sustainable pathway that bypasses external electrical energy.

In summary, GDY has emerged as a genuinely active carbon platform that redefines the role of carbon in catalysis. The foundational principles established over the past decade have firmly validated its potential for sustainable ammonia synthesis. This review provides a comprehensive framework and a clear roadmap to guide the transition of green ammonia synthesis from laboratory research to practical application, offering new strategies to reduce energy consumption and carbon emissions associated with the traditional Haber-Bosch process.

DECLARATIONS

Authors' contributions

Made substantial contributions to conception and design of the study: Wang, S.
Performed data acquisition: Wang, G.; Xiao, H.; Wu, H.
Provided administrative, technical, and material support: Xue, Y.

Availability of data and materials

Not applicable.

AI and AI-assisted tools statement

Not applicable.

Financial support and sponsorship

This work was supported by the National Key Research and Development Project of China (No. 2024YFA1509400), the National Natural Science Foundation of China (No. 22575095), and the Natural Science Foundation of Shandong Province (ZR2024ZD02).

Conflicts of interest

All authors declared that there are no conflicts of interest.

Ethical approval and consent to participate

Not applicable.

Consent for publication

Not applicable.

REFERENCES

1. Ye, T. N.; Park, S. W.; Lu, Y.; et al. Vacancy-enabled N_2 activation for ammonia synthesis on an Ni-loaded catalyst. *Nature* **2020**, *583*, 391-5. DOI PubMed
2. Ampelli, C. Electrode design for ammonia synthesis. *Nat. Catal.* **2020**, *3*, 420-1. DOI
3. Mallick, A.; Mayorga-Martinez, C. C.; Pumera, M. Low-dimensional materials for ammonia synthesis. *Chem. Soc. Rev.* **2025**, *54*, 5021-80. DOI PubMed
4. Liang, J.; Li, Z.; Zhang, L.; et al. Advances in ammonia electrosynthesis from ambient nitrate/nitrite reduction. *Chem* **2023**, *9*, 1768-827. DOI
5. Ai, X.; Chen, H.; Liang, X.; et al. Metal-coordinating single-boron sites confined in antiperovskite borides for N_2-to-NH_3 catalytic conversion. *ACS. Catal.* **2022**, *12*, 2967-78. DOI
6. Li, S.; Fu, X.; Nørskov, J. K.; Chorkendorff, I. Towards sustainable metal-mediated ammonia electrosynthesis. *Nat. Energy.* **2024**, *9*, 1344-9. DOI
7. Wang, P.; Chang, F.; Gao, W.; et al. Breaking scaling relations to achieve low-temperature ammonia synthesis through LiH-mediated nitrogen transfer and hydrogenation. *Nat. Chem.* **2017**, *9*, 64-70. DOI PubMed
8. Zhang, N.; Jalil, A.; Wu, D.; et al. Refining defect states in $W_{18}O_{49}$ by mo doping: a strategy for tuning N_2 activation towards solar-driven nitrogen fixation. *J. Am. Chem. Soc.* **2018**, *140*, 9434-43. DOI PubMed
9. Ye, D.; Tsang, S. C. E. Prospects and challenges of green ammonia synthesis. *Nat. Synth.* **2023**, *2*, 612-23. DOI
10. Jiao, F.; Xu, B. Electrochemical ammonia synthesis and ammonia fuel cells. *Adv. Mater.* **2019**, *31*, e1805173. DOI PubMed
11. Wu, T.; Fan, W.; Zhang, Y.; Zhang, F. Electrochemical synthesis of ammonia: progress and challenges. *Mater. Today. Phys.* **2021**, *16*, 100310. DOI
12. Chen, Y.; Guo, R.; Peng, X.; et al. Highly productive electrosynthesis of ammonia by admolecule-targeting single Ag sites. *ACS. Nano.* **2020**, *14*, 6938-46. DOI PubMed
13. Li, J.; Jiang, Y.; Zhang, Z.; et al. Barium oxynitride electride as highly enhanced promotor for ruthenium catalyst in ammonia synthesis: comparative study with barium oxide. *Adv. Energy. Mater.* **2023**, *13*, 2302424. DOI
14. Li, R.; Xiang, K.; Peng, Z.; Zou, Y.; Wang, S. Recent advances on electrolysis for simultaneous generation of valuable chemicals at both anode and cathode. *Adv. Energy. Mater.* **2021**, *11*, 2102292. DOI
15. Yu, J.; Xi, Z.; Su, J.; et al. Influence of active hydrogen on pathway selection in electrochemical nitrate reduction. *eScience* **2025**, *5*, 100350. DOI
16. Gao, W.; Guo, J.; Wang, P.; et al. Production of ammonia via a chemical looping process based on metal imides as nitrogen carriers. *Nat. Energy.* **2018**, *3*, 1067-75. DOI

17. Lan, Y. Y.; Chen, W. X.; Si, D. H.; et al. Metal-organic framework glass-based self-supporting electrodes for efficient electrocatalytic nitrate reduction to ammonia. *CCS. Chem.* **2026**, *8*, 1997-2010. DOI
18. Chen, T.; Wang, L.; Liang, C.; et al. Functional nanomaterials with tip effect: synthesis and applications in electrocatalysis. *CCS. Chem.* **2026**, *8*, 14-36. DOI
19. Jia, S.; Zhao, K.; Han, L.; et al. Towards green chemistry from transformation of carbon dioxide and dinitrogen to value-added chemicals and fuels. *Sci. Bull.* **2025**, *70*, 3420-38. DOI PubMed
20. Liu, H.; Guo, X.; Wang, L.; et al. Hydroxide-activated hydrogen spillover-mediated nitrogen reduction pathways for efficient ammonia synthesis. *eScience* **2026**, *6*, 100513. DOI
21. Tan, Y.; Zhao, Y.; Chen, X.; et al. Cooperative Cu with defective MXene for enhanced nitrate electroreduction to ammonia. *EcoEnergy* **2024**, *2*, 258-67. DOI
22. Feng, Y.; Ren, J. T.; Song, Y. X.; et al. Super-hydrophilic/aerophobic $Co(OH)_2$/NiFe layered double hydroxide heterostructures with moderate work function difference for large-current-density electrochemical ammonia synthesis. *CCS. Chem.* **2025**, *7*, 1344-58. DOI
23. Wei, Y.; Cheng, G.; Li, L.; et al. In situ dynamic reconstruction of Co_3 Mo electrocatalyst for efficient nitrate reduction to ammonia. *Adv. Funct. Mater.* **2026**, *36*, e75762. DOI
24. Singh, A. R.; Rohr, B. A.; Schwalbe, J. A.; et al. Electrochemical ammonia synthesis - the selectivity challenge. *ACS. Catal.* **2017**, *7*, 706-9. DOI
25. Wei, X.; Chen, C.; Fu, X. Z.; Wang, S. Oxygen Vacancies-rich metal oxide for electrocatalytic nitrogen cycle. *Adv. Energy. Mater.* **2023**, *14*, 2303027. DOI
26. Klein, C. K.; Manthiram, K. Sustainable ammonia synthesis: just around the corner? *Joule* **2022**, *6*, 1971-3. DOI
27. Mu, B. S.; Xu, Y.; Tu, Z.; et al. Radiocatalytic ammonia synthesis from nitrogen and water. *Natl. Sci. Rev.* **2024**, *11*, nwae302. DOI PubMed PMC
28. Fu, Y.; Zhu, S.; Song, Y.; Wei, P.; Wang, G.; Bao, X. Sustainable electrochemical ammonia synthesis mediated by nitrogen oxides. *CCS. Chem.* **2026**, *8*, 1780-90. DOI
29. Zhang, L.; Ji, X.; Ren, X.; et al. Electrochemical ammonia synthesis via nitrogen reduction reaction on a MoS_2 catalyst: theoretical and experimental studies. *Adv. Mater.* **2018**, *30*, e1800191. DOI PubMed
30. Wang, Q.; Pan, J.; Guo, J.; et al. Ternary ruthenium complex hydrides for ammonia synthesis via the associative mechanism. *Nat. Catal.* **2021**, *4*, 959-67. DOI
31. Weber, J. E.; Mcmillion, N. D.; Hegg, A. S.; et al. Isocyanide ligation enables electrochemical ammonia formation in a synthetic cycle for N_2 fixation. *J. Am. Chem. Soc.* **2024**, *146*, 33595-607. DOI PubMed
32. Chang, F.; Gao, W.; Guo, J.; Chen, P. Emerging materials and methods toward ammonia-based energy storage and conversion. *Adv. Mater.* **2021**, *33*, e2005721. DOI PubMed
33. Daisley, A.; Hargreaves, J. S. J. Chemical capacitors for ammonia synthesis. *Nat. Catal.* **2025**, *8*, 200-1. DOI
34. Andersen, S. Z.; Čolić, V.; Yang, S.; et al. A rigorous electrochemical ammonia synthesis protocol with quantitative isotope measurements. *Nature* **2019**, *570*, 504-8. DOI PubMed
35. Guo, H.; Zhang, X.; Lyu, J.; et al. Constructing asymmetrically coordinated transition metal single atoms with high loadings for ammonia electrosynthesis. *Nat. Synth.* **2026**, Epub ahead of print. DOI
36. Kibsgaard, J.; Nørskov, J. K.; Chorkendorff, I. The difficulty of proving electrochemical ammonia synthesis. *ACS. Energy. Lett.* **2019**, *4*, 2986-8. DOI
37. Bruch, Q. J.; Connor, G. P.; Chen, C.; et al. Dinitrogen reduction to ammonium at rhenium utilizing light and proton-coupled electron transfer. *J. Am. Chem. Soc.* **2019**, *141*, 20198-208. DOI PubMed
38. Liu, S.; Wang, M.; Ji, H.; Shen, X.; Yan, C.; Qian, T. Altering the rate-determining step over cobalt single clusters leading to highly efficient ammonia synthesis. *Natl. Sci. Rev.* **2021**, *8*, nwaa136. DOI PubMed PMC
39. Liao, G. Smith Jr., R. L.; Guo, H.; Qi, X. Review of carbon-based catalysts for electrochemical nitrate reduction and green ammonia synthesis. *Green. Chem.* **2024**, *26*, 11797-831. DOI
40. Titirici, M. M.; White, R. J.; Brun, N.; et al. Sustainable carbon materials. *Chem. Soc. Rev.* **2015**, *44*, 250-90. DOI PubMed
41. Valentini, F.; Grigoras, A. M.; Vaccaro, L.; Latterini, L. Sustainable nitrogen photofixation: considerations on the state of the art of non critical carbon materials. *Carbon. Energy.* **2024**, *6*, e545. DOI
42. Masood ul Hasan, I. M.; Liu, Y.; Nawaz, M. Z.; et al. Trends and prospects in electrochemical nitrate-to-ammonia conversion: Emphasis on carbon-based metal-free catalysts. *Renew. Sustain. Energy. Rev.* **2026**, *234*, 116935. DOI
43. Zhang, G.; Li, Y.; He, C.; Ren, X.; Zhang, P.; Mi, H. Recent progress in 2D catalysts for photocatalytic and electrocatalytic artificial nitrogen reduction to ammonia. *Adv. Energy. Mater.* **2021**, *11*, 2003294. DOI

44. Wang, D. Y.; Gong, M.; Chou, H. L.; et al. Highly active and stable hybrid catalyst of cobalt-doped FeS_2 nanosheets-carbon nanotubes for hydrogen evolution reaction. *J. Am. Chem. Soc.* **2015**, *137*, 1587-92. DOI PubMed
45. Wu, K.; Qiu, X.; Luo, Y.; Zhang, C. Oxygen vacancy mediated-bismuth molybdate/graphitic carbon nitride type II heterojunction chemiresistor for efficient NH_3 detection at room temperature. *ACS. Sens.* **2024**, *9*, 6698-708. DOI PubMed
46. Xu, Z.; Deng, W.; Wang, X. 3D Hierarchical carbon-rich micro-/nanomaterials for energy storage and catalysis. *Electrochem. Energ. Rev.* **2021**, *4*, 269-335. DOI
47. Zhu, Z.; Men, Y.; Zhang, W.; et al. Versatile carbon-based materials from biomass for advanced electrochemical energy storage systems. *eScience* **2024**, *4*, 100249. DOI
48. Zhang, W.; Zhan, S.; Qin, Q.; et al. Electrochemical generation of catalytically active edge sites in C_2N-type carbon materials for artificial nitrogen fixation. *Small* **2022**, *18*, e2204116. DOI PubMed
49. Wu, Q.; Yan, X.; Jia, Y.; Yao, X. Defective carbon-based materials: controllable synthesis and electrochemical applications. *EnergyChem* **2021**, *3*, 100059. DOI
50. Li, G.; Li, Y.; Liu, H.; Guo, Y.; Li, Y.; Zhu, D. Architecture of graphdiyne nanoscale films. *Chem. Commun.* **2010**, *46*, 3256-8. DOI PubMed
51. Sun, Q.; Lu, T.; He, J.; Huang, C. Advances in the study of heteratomic graphdiyne electrode materials. *Chem. J. Chinese. Univ.* **2021**, *42*, 366. DOI
52. Ge, C.; Chen, J.; Tang, S.; Du, Y.; Tang, N. Review of the electronic, optical, and magnetic properties of graphdiyne: from theories to experiments. *ACS. Appl. Mater. Interfaces.* **2019**, *11*, 2707-16. DOI PubMed
53. Zhang, Y.; Huang, P.; Guo, J.; et al. Graphdiyne-based flexible photodetectors with high responsivity and detectivity. *Adv. Mater.* **2020**, *32*, e2001082. DOI PubMed
54. Gao, X.; Liu, H.; Wang, D.; Zhang, J. Graphdiyne: synthesis, properties, and applications. *Chem. Soc. Rev.* **2019**, *48*, 908-36. DOI PubMed
55. Fang, Y.; Liu, Y.; Qi, L.; Xue, Y.; Li, Y. 2D graphdiyne: an emerging carbon material. *Chem. Soc. Rev.* **2022**, *51*, 2681-709. DOI PubMed
56. Li, J.; Gao, X.; Zhu, L.; et al. Graphdiyne for crucial gas involved catalytic reactions in energy conversion applications. *Energy. Environ. Sci.* **2020**, *13*, 1326-46. DOI
57. Liang, S.; Deng, H.; Zhou, Z.; Wong, W. Y. Fabrication of graphdiyne and its analogues for photocatalytic application. *EcoMat* **2022**, *5*, e12297. DOI
58. Nidhi, H. V.; Koppad, V. S.; Babu, A. M.; Varghese, A. Properties, synthesis and emerging applications of graphdiyne: a journey through recent advancements. *Top. Curr. Chem.* **2024**, *382*, 19. DOI PubMed
59. Yang, B.; Jin, F.; Jin, Z.; Tsubaki, N. Directional electron transfer via Cu_3P-graphdiyne-$Ni_3SbS_{6-\delta}$ interface: role of ohmic contact and graphdiyne synergy in boosting photocatalytic hydrogen evolution. *Appl. Catal. B:. Environ. Energy.* **2025**, *378*, 125624. DOI
60. Jia, Z.; Li, Y.; Zuo, Z.; Liu, H.; Huang, C.; Li, Y. Synthesis and properties of 2D carbon - graphdiyne. *Acc. Chem. Res.* **2017**, *50*, 2470-8. DOI PubMed
61. Yang, Z.; Zhang, D.; Wang, K.; He, J.; Li, J.; Huang, C. Investigating graphdiyne based materials for rechargeable batteries. *Nano. Today.* **2022**, *46*, 101588. DOI
62. Wu, X.; Lu, Y.; Li, P.; et al. Current advances in the synthesis, properties, and biomedical applications of two-dimensional graphdiyne: a review. *ACS. Appl. Nano. Mater.* **2024**, *7*, 2461-93. DOI
63. Han, Y. Y.; Lu, X. L.; Tang, S. F.; Yin, X. P.; Wei, Z. W.; Lu, T. B. Metal-free 2D/2D heterojunction of graphitic carbon nitride/graphdiyne for improving the hole mobility of graphitic carbon nitride. *Adv. Energy. Mater.* **2018**, *8*, 1702992. DOI
64. Zhao, Y.; Yang, N.; Yu, R.; et al. Unique structural advances of graphdiyne for energy applications. *EnergyChem* **2020**, *2*, 100041. DOI
65. Tang, S. F.; Lu, X. L.; Zhang, C.; Wei, Z. W.; Si, R.; Lu, T. B. Decorating graphdiyne on ultrathin bismuth subcarbonate nanosheets to promote CO_2 electroreduction to formate. *Sci. Bull.* **2021**, *66*, 1533-41. DOI PubMed
66. Yu, J.; Cao, C.; Jin, H.; et al. Uniform single atomic Cu_1-C_4 sites anchored in graphdiyne for hydroxylation of benzene to phenol. *Natl. Sci. Rev.* **2022**, *9*, nwac018. DOI PubMed PMC
67. Du, Y.; Zhou, W.; Gao, J.; Pan, X.; Li, Y. Fundament and application of graphdiyne in electrochemical energy. *Acc. Chem. Res.* **2020**, *53*, 459-69. DOI PubMed
68. Kong, Y.; Li, J.; Zeng, S.; Yin, C.; Tong, L.; Zhang, J. Bridging the gap between reality and ideality of graphdiyne: the advances of synthetic methodology. *Chem* **2020**, *6*, 1933-51. DOI
69. Qi, R.; Wang, D.; Lu, X. Heterojunction engineering in electrocatalytic nitrate-to-ammonia conversion. *Coord. Chem. Rev.* **2026**, *551*, 217483. DOI

70. Khan, K.; Tareen, A. K.; Iqbal, M.; Shi, Z.; Zhang, H.; Guo, Z. Novel emerging graphdiyne based two dimensional materials: Synthesis, properties and renewable energy applications. *Nano. Today.* **2021**, *39*, 101207. DOI
71. Hui, L.; Xue, Y.; Yu, H.; et al. Highly efficient and selective generation of ammonia and hydrogen on a graphdiyne-based catalyst. *J. Am. Chem. Soc.* **2019**, *141*, 10677-83. DOI PubMed
72. Yu, H.; Xue, Y.; Hui, L.; et al. Graphdiyne-based metal atomic catalysts for synthesizing ammonia. *Natl. Sci. Rev.* **2021**, *8*, nwaa213. DOI PubMed PMC
73. Zou, H.; Rong, W.; Wei, S.; Ji, Y.; Duan, L. Regulating kinetics and thermodynamics of electrochemical nitrogen reduction with metal single-atom catalysts in a pressurized electrolyser. *Proc. Natl. Acad. Sci. U. S. A.* **2020**, *117*, 29462-8. DOI PubMed PMC
74. Feng, X.; Liu, J.; Chen, L.; et al. Hydrogen radical-induced electrocatalytic N_2 reduction at a low potential. *J. Am. Chem. Soc.* **2023**, *145*, 10259-67. DOI PubMed
75. Feng, B.; Zhang, D.; Han, Z.; et al. Rational synthesis of isomeric graphdiyne frameworks toward single-ruthenium catalysts and high-performance nitrogen reduction. *Adv. Mater.* **2025**, *37*, e2502980. DOI PubMed
76. Zou, H.; Arachchige, L. J.; Rong, W.; et al. Low-valence metal single atoms on graphdiyne promotes electrochemical nitrogen reduction via M-to-N_2 π-backdonation. *Adv. Funct. Mater.* **2022**, *32*, 2200333. DOI
77. Fang, Y.; Xue, Y.; Hui, L.; Chen, X.; Li, Y. High-loading metal atoms on graphdiyne for efficient nitrogen fixation to ammonia. *J. Mater. Chem. A.* **2022**, *10*, 6073-7. DOI
78. Guo, Y.; Liu, J.; Yang, Q.; et al. Regulating nitrogenous adsorption and desorption on Pd clusters by the acetylene linkages of hydrogen substituted graphdiyne for efficient electrocatalytic ammonia synthesis. *Nano. Energy.* **2021**, *86*, 106099. DOI
79. Xing, C.; Wu, C.; Xue, Y.; et al. A highly selective and active metal-free catalyst for ammonia production. *Nanoscale. Horiz.* **2020**, *5*, 1274-8. DOI PubMed
80. Yang, Q.; Guo, Y.; Gu, J.; et al. Scalable synthesis of 2D hydrogen-substituted graphdiyne on Zn substrate for high-yield N_2 fixation. *Nano. Energy.* **2020**, *78*, 105283. DOI
81. Zou, H.; Rong, W.; Long, B.; Ji, Y.; Duan, L. Corrosion-induced Cl-doped ultrathin graphdiyne toward electrocatalytic nitrogen reduction at ambient conditions. *ACS. Catal.* **2019**, *9*, 10649-55. DOI
82. Fang, Y.; Xue, Y.; Hui, L.; et al. Graphdiyne-induced iron vacancy for efficient nitrogen conversion. *Adv. Sci.* **2022**, *9*, e2102721. DOI PubMed PMC
83. Fang, Y.; Xue, Y.; Li, Y.; et al. Graphdiyne interface engineering: highly active and selective ammonia synthesis. *Angew. Chem. Int. Ed. Engl.* **2020**, *59*, 13021-7. DOI PubMed
84. Zhou, X.; Wu, W.; Xu, D.; Liu, C.; Zhang, Z. Bioinspired dual-site photocathode with atomic molybdenum and alkynyl networks for scalable solar ammonia synthesis. *ACS. Nano.* **2025**, *19*, 19417-28. DOI PubMed
85. Feng, X.; Liu, J.; Kong, Y.; et al. Cu/Cu_xO/Graphdiyne tandem catalyst for efficient electrocatalytic nitrate reduction to ammonia. *Adv. Mater.* **2024**, *36*, e2405660. DOI PubMed
86. Wu, H.; Gao, Y.; Zheng, X.; et al. Controlled growth of $PtCu_x$ quantum dots on graphdiyne for efficient ammonia production. *ACS. Mater. Lett.* **2024**, *6*, 2787-93. DOI
87. Wang, C.; Song, T.; Dai, H.; et al. Electronic perturbation of Pd single-atom catalysts on graphdiyne derivatives toward effective electrocatalytic nitrate reduction. *ChemPhysMater* **2025**, *4*, 321-9. DOI
88. Zheng, Z.; Qi, L.; Xue, Y.; Li, Y. Highly selective and durable of monodispersed metal atoms in ammonia production. *Nano. Today.* **2022**, *43*, 101431. DOI
89. Zhang, Z.; Feng, X.; Zhang, Z.; et al. Graphdiyne enabled nitrogen vacancy formation in copper nitride for efficient ammonia synthesis. *J. Am. Chem. Soc.* **2024**, *146*, 14898-904. DOI PubMed
90. Kuang, J.; Yu, J.; Zhang, Q.; et al. Graphdiyne production in a flash: high-yield direct synthesis by electron beam irradiation. *Adv. Mater.* **2025**, *37*, e2506979. DOI PubMed
91. Li, J.; Valenza, R.; Haussener, S. In situ synthesis of Cu_xO/N doped graphdiyne with pyridine N configuration for ammonia production via nitrate reduction. *Small* **2024**, *20*, e2310467. DOI PubMed
92. Luan, X.; Qi, L.; Zhao, S.; Chen, Z.; Xue, Y. Controllable assembly of planar defect-rich bimetallic oxide interfaces for efficient ammonia production. *Small. Methods.* **2026**, *10*, e2500957. DOI PubMed
93. Chen, Z.; Zhao, S.; Luan, X.; Zheng, Z.; Yan, J.; Xue, Y. A Co_3O_4/graphdiyne heterointerface for efficient ammonia production from nitrates. *New. Carbon. Mater.* **2024**, *39*, 142-51. DOI
94. Zheng, X.; Xue, Y.; Zhang, C.; Li, Y. Controlled growth of multidimensional interface for high-selectivity ammonia production. *CCS. Chem.* **2023**, *5*, 1653-62. DOI
95. Luan, X.; Qi, L.; Zheng, Z.; et al. *In situ* growth of a GDY-MnO_x heterointerface for selective and efficient ammonia production. *Chem. Commun.* **2023**, *59*, 7611-4. DOI PubMed

96. Zhao, S.; Zheng, Z.; Qi, L.; Xue, Y.; Li, Y. Controlled growth of donor-bridge-acceptor interface for high-performance ammonia production. *Small* **2022**, *18*, e2107136. DOI PubMed
97. Wang, B.; Ma, J.; Yang, R.; et al. Bridging nickel-MOF and copper single atoms/clusters with H-substituted graphdiyne for the tandem catalysis of nitrate to ammonia. *Angew. Chem. Int. Ed. Engl.* **2024**, *63*, e202404819. DOI PubMed
98. Ma, J.; Zhang, Y.; Wang, B.; Jiang, Z.; Zhang, Q.; Zhuo, S. Interfacial engineering of bimetallic Ni/Co-MOFs with H-substituted graphdiyne for ammonia electrosynthesis from nitrate. *ACS. Nano.* **2023**, *17*, 6687-97. DOI PubMed
99. Gao, Y.; Liu, H.; Zheng, Z.; Luan, X.; Xue, Y.; Li, Y. Controlled growth of a graphdiyne-Prussian blue analog heterostructure for efficient ammonia production. *NPG. Asia. Mater.* **2023**, *15*, 12. DOI
100. Ma, J.; Wang, R.; Wang, B.; Luo, J.; Zhang, Q.; Zhuo, S. Hybrid nanoarrays of Cu-MOFs@H-substituted graphdiyne with various levels of Lewis acidity for nitrate electroreduction. *Chem. Commun.* **2023**, *59*, 4348-51. DOI PubMed
101. Fu, X.; Zhao, X.; Lu, T. B.; Yuan, M.; Wang, M. Graphdiyne-based single-atom catalysts with different coordination environments. *Angew. Chem. Int. Ed. Engl.* **2023**, *62*, e202219242. DOI PubMed
102. Zheng, X.; Chen, S.; Li, J.; et al. Two-dimensional carbon graphdiyne: advances in fundamental and application research. *ACS. Nano.* **2023**, *17*, 14309-46. DOI PubMed
103. Wu, R.; Huang, C.; Li, Y. Emerging electrochemical energy conversion materials: graphdiyne. *Adv. Mater.* **2026**, e00027. DOI PubMed
104. Zhan, S.; Zhao, Y.; Yang, N.; Wang, D. Pore structure of graphdiyne: design, synthesis and application. *Chem. J. Chinese. Univ.* **2021**, *42*, 333. DOI
105. Wang, H.; Zhang, X.; Liu, J.; Chen, C. Modulating the electronic structure of graphdiyne-based nanomaterials for engineering nano-bio interfaces in biomedical applications. *Adv. Drug. Deliv. Rev.* **2025**, *220*, 115570. DOI PubMed
106. Wu, T.; Sun, M.; Huang, B. Graphdiyne based catalysts for energy applications. *Mater. Chem. Front.* **2021**, *5*, 7369-83. DOI
107. Do, D. P.; Lee, E.; Bui, V. Q.; Lee, H. Recent progress in two-dimensional graphdiyne: synthesis, characterization, and applications. *ChemPhysMater* **2025**, *4*, 91-107. DOI
108. Ansari, M. Z.; Ansari, S. A.; Parveen, N.; et al. Exploring graphdiyne, MXene, borophene, and phosphorene as advanced 2D materials for next-generation metallic ion batteries. *Prog. Mater. Sci.* **2026**, *158*, 101617. DOI
109. Huang, C.; Li, Y.; Wang, N.; et al. Progress in research into 2D graphdiyne-based materials. *Chem. Rev.* **2018**, *118*, 7744-803. DOI PubMed
110. Yu, H.; Xue, Y.; Li, Y. Graphdiyne and its assembly architectures: synthesis, functionalization, and applications. *Adv. Mater.* **2019**, *31*, 1803101. DOI PubMed
111. Liu, B.; Xu, L.; Zhao, Y.; Du, J.; Yang, N.; Wang, D. Heteroatoms in graphdiyne for catalytic and energy-related applications. *J. Mater. Chem. A.* **2021**, *9*, 19298-316. DOI
112. Chen, H.; Liu, X.; Gong, D.; et al. Ultrahigh-water-flux desalination on graphdiyne membranes. *Nat. Water.* **2023**, *1*, 800-7. DOI
113. Xie, H.; Jia, P.; Huang, H. Multidimensional graphdiyne structures and beyond for energy conversion and storage. *Adv. Funct. Mater.* **2025**, *36*, e10586. DOI
114. Liu, X.; Zhao, Y.; Du, J.; Wang, D. Recent progress and challenges in crystalline graphdiyne. *Sci. China. Mater.* **2024**, *67*, 729-51. DOI
115. Yin, X. P.; Wang, H. J.; Tang, S. F.; et al. Engineering the coordination environment of single-atom platinum anchored on graphdiyne for optimizing electrocatalytic hydrogen evolution. *Angew. Chem. Int. Ed. Engl.* **2018**, *57*, 9382-6. DOI PubMed
116. Gao, Y.; Xue, Y.; Wu, H.; et al. Self-organized gradually single-atom-layer of metal osmium for an unprecedented hydrogen production from seawater. *J. Am. Chem. Soc.* **2024**, *146*, 10573-80. DOI PubMed
117. Xue, Y.; Huang, B.; Yi, Y.; et al. Anchoring zero valence single atoms of nickel and iron on graphdiyne for hydrogen evolution. *Nat. Commun.* **2018**, *9*, 1460. DOI PubMed PMC
118. Zhang, S.; Kong, Y.; Gu, Y.; et al. Strong d-π orbital coupling of Co-C_4 atomic sites on graphdiyne boosts potassium-sulfur battery electrocatalysis. *J. Am. Chem. Soc.* **2024**, *146*, 4433-43. DOI PubMed
119. Zhang, L.; Li, J.; Wei, G.; Yang, H.; Bai, H.; Xi, G. Exploring the fate of copper ions in the synthesis of graphdiyne. *Angew. Chem. Int. Ed. Engl.* **2024**, *63*, e202316936. DOI PubMed
120. Wu, R.; Fu, X.; Huang, C.; Gao, J.; Yang, J.; Li, Y. Recent progress in the preparation of graphdiyne-based materials. *ChemistryEurope* **2025**, *3*, e202500141. DOI
121. Sakamoto, R.; Fukui, N.; Maeda, H.; Matsuoka, R.; Toyoda, R.; Nishihara, H. The accelerating world of graphdiynes. *Adv. Mater.* **2019**, *31*, e1804211. DOI PubMed
122. Zhang, W.; Xu, J.; Wang, T.; Lin, X.; Wang, F. Graphdiyne as an emerging sensor platform: principles, synthesis and application. *J. Adv. Res.* **2025**, *74*, 283-301. DOI PubMed PMC
123. Yu, M.; He, J.; Hu, X.; et al. Graphdiyne and its derivatives: a stabilizer for metastable particles. *Adv. Compos. Hybrid. Mater.* **2025**, *8*, 377. DOI

124. Yu, S.; Chen, J.; Chen, C.; et al. What happens when graphdiyne encounters doping for electrochemical energy conversion and storage. *Coord. Chem. Rev.* **2023**, *482*, 215082. DOI
125. Peng, J.; Tian, Z.; Zhao, T.; Shang, H.; Wu, J. Recent progress in preparations and multifunctional applications towards MOF/GDY composites and their derivative materials. *Catalysts* **2025**, *15*, 1041. DOI
126. Zhu, C.; Fu, S.; Shi, Q.; Du, D.; Lin, Y. Single-atom electrocatalysts. *Angew. Chem. Int. Ed. Engl.* **2017**, *56*, 13944-60. DOI PubMed
127. Han, C.; Zhang, S.; Zhang, H.; et al. Metal-support interaction in single-atom electrocatalysts: a perspective of metal oxide supports. *eScience* **2024**, *4*, 100269. DOI
128. Gao, Y.; Wang, D. Atomically dispersed catalysts: precise synthesis, structural regulation, and structure-activity relationship. *CCS. Chem.* **2024**, *6*, 833-55. DOI
129. Bi, W.; Shaigan, N.; Malek, A.; Fatih, K.; Gyenge, E.; Wilkinson, D. P. Strategies in cell design and operation for the electrosynthesis of ammonia: status and prospects. *Energy. Environ. Sci.* **2022**, *15*, 2259-87. DOI
130. Qing, G.; Ghazfar, R.; Jackowski, S. T.; et al. Recent advances and challenges of electrocatalytic N_2 reduction to ammonia. *Chem. Rev.* **2020**, *120*, 5437-516. DOI PubMed
131. Song, T.; Liu, X.; Zhu, Y. Toward fundamental insights into heterogeneous catalysis by supported atomically precise metal clusters. *CCS. Chem.* **2026**, *8*, 1175-203. DOI
132. Ying, Y.; Fan, K.; Qiao, J.; Huang, H. Rational design of atomic site catalysts for electrocatalytic nitrogen reduction reaction: one step closer to optimum activity and selectivity. *Electrochem. Energy. Rev.* **2022**, *5*, 6. DOI
133. Tang, T.; Bai, X.; Wang, Z.; Guan, J. Structural engineering of atomic catalysts for electrocatalysis. *Chem. Sci.* **2024**, *15*, 5082-112. DOI PubMed PMC
134. Zhang, M.; Ji, S.; Zhang, Z.; Zhu, M.; Yao, Q.; Xie, J. Engineering surface structure of atomically precise metal nanoclusters at the molecular level. *CCS. Chem.* **2026**, *8*, 37-59. DOI
135. Wong, H.; Lu, Q.; Sun, M.; Huang, B. Rational design of graphdiyne-based atomic electrocatalysts: DFT and self-validated machine learning. *Chem. J. Chinese. Univ.* **2022**, *43*, 20220042. DOI
136. Zhao, M.; Jiang, L.; Yu, Q. Environmental applications of single-atom catalysts based on graphdiyne. *Catal. Sci. Technol.* **2023**, *13*, 5154-74. DOI
137. Kan, X.; Fan, C.; Wu, C.; Sun, C.; Li, Z.; Zhao, Y. Graphdiyne-supported atomic catalysts: synthesis and applications. *ChemPlusChem* **2020**, *85*, 2570-9. DOI PubMed
138. Li, B.; Lai, C.; Zhang, M.; et al. Graphdiyne: a rising star of electrocatalyst support for energy conversion. *Adv. Energy. Mater.* **2020**, *10*, 2000177. DOI
139. Xiong, S.; Wang, W.; Wang, F.; et al. Thermal catalytic synthesis of ammonia using uranium/graphdiyne composite at mild conditions. *Nat. Commun.* **2026**, *17*, 2894. DOI PubMed PMC
140. Jin, R.; Xu, X.; Xia, Y.; et al. Robust oxygen reduction electrocatalysis via dioxygen-bridged cobalt diatomic sites scaffolded by hierarchically porous nanoarchitectures. *Sci. Bull.* **2026**, *71*, 2012-21. DOI PubMed
141. Dong, X. Y.; Jin, Y. J.; Chen, H.; Li, B.; Zang, S. Q.; Cai, J. Atomic-level dynamic spacing engineering in COF-based electrocatalysts for urea synthesis in ultra-low and wide potential ranges. *Sci. Bull.* **2026**, *71*, 1380-6. DOI PubMed
142. Liu, S.; Lu, J.; Yu, X.; Pang, H.; Zhang, Q.; Park, H. S. Rational design of metal-organic framework-nanoparticle composite electrocatalysts for sustainable nitrogen electrochemistry. *eScience* **2025**, *5*, 100378. DOI
143. He, B.; Ren, M.; Zhang, L.; et al. Breaking scaling relations and boosting ammonia synthesis in nitrogen reduction with V-containing heteronuclear double metal atoms. *J. Mater. Chem. A.* **2025**, *13*, 2093-104. DOI
144. Wang, X.; Yang, L. Composition engineering opens an avenue toward efficient and sustainable nitrogen fixation. *Energy. Environ. Mater.* **2023**, *7*, e12600. DOI
145. Ma, D.; Zeng, Z.; Liu, L.; Jia, Y. Theoretical screening of the transition metal heteronuclear dimer anchored graphdiyne for electrocatalytic nitrogen reduction. *J. Energy. Chem.* **2021**, *54*, 501-9. DOI
146. Luo, Y.; Li, M.; Dai, Y.; et al. Transition metal-modified Co_4 clusters supported on graphdiyne as an effective nitrogen reduction reaction electrocatalyst. *Inorg. Chem.* **2021**, *60*, 18251-9. DOI PubMed
147. Jasin Arachchige, L.; Xu, Y.; Dai, Z.; Zhang, X. L.; Wang, F.; Sun, C. Double transition metal atoms anchored on Graphdiyne as promising catalyst for electrochemical nitrogen reduction reaction. *J. Mater. Sci. Technol.* **2021**, *77*, 244-51. DOI
148. Ma, D.; Zeng, Z.; Liu, L.; Huang, X.; Jia, Y. Computational evaluation of electrocatalytic nitrogen reduction on TM single-, double-, and triple-atom catalysts (TM = Mn, Fe, Co, Ni) based on graphdiyne monolayers. *J. Phys. Chem. C.* **2019**, *123*, 19066-76. DOI
149. Li, M.; Cui, Y.; Zhang, X.; Luo, Y.; Dai, Y.; Huang, Y. Screening a suitable Mo form supported on graphdiyne for effectively electrocatalytic N_2 reduction reaction: from atomic catalyst to cluster catalyst. *J. Phys. Chem. Lett.* **2020**, *11*, 8128-37. DOI PubMed

150. Chen, Z. W.; Chen, L. X.; Jiang, M.; et al. A triple atom catalyst with ultrahigh loading potential for nitrogen electrochemical reduction. *J. Mater. Chem. A.* **2020**, *8*, 15086-93. DOI
151. Fu, C.; Li, Y.; Wei, H. Double boron atom-doped graphdiynes as efficient metal-free electrocatalysts for nitrogen reduction into ammonia: a first-principles study. *Phys. Chem. Chem. Phys.* **2021**, *23*, 17683-92. DOI PubMed
152. Wang, Q. Y.; Xie, X. Y.; Zhou, H.; et al. Efficient NRR on S, N-doped/adsorbed graphdiyne: a density functional theory investigation. *Mol. Catal.* **2026**, *601*, 116092. DOI
153. Wang, G.; Cai, W.; Fan, T.; Ji, Y. Nitrogen-doped graphdiyne for efficient electrocatalytic N_2 reduction: a first-principles study. *Appl. Surf. Sci.* **2021**, *570*, 151109. DOI
154. Cheng, Y.; Chen, W.; He, C.; Zhang, W. New insights into the long-range interaction mechanism of nitrogen reduction. *J. Energy. Chem.* **2025**, *106*, 842-51. DOI
155. Feng, Z.; Tang, Y.; Chen, W.; Wei, D.; Ma, Y.; Dai, X. O-doped graphdiyne as metal-free catalysts for nitrogen reduction reaction. *Mol. Catal.* **2020**, *483*, 110705. DOI
156. Fu, C.; Li, Y.; Wei, H. Single boron modulated graphdiyne nanosheets for efficient electrochemical nitrogen fixation: a first-principles study. *Phys. Chem. Chem. Phys.* **2022**, *24*, 19817-26. DOI PubMed
157. Zheng, X.; Gao, X.; Vilá, R. A.; et al. Hydrogen-substituted graphdiyne-assisted ultrafast sparking synthesis of metastable nanomaterials. *Nat. Nanotechnol.* **2023**, *18*, 153-9. DOI PubMed
158. Cui, C.; Jia, Y.; Zhang, H.; Geng, L.; Luo, Z. Plasma-assisted dinitrogen activation via dual platinum cluster catalysis: a strategy for ammonia synthesis under mild conditions. *CCS. Chem.* **2023**, *5*, 682-94. DOI
159. Gao, X.; Li, J.; Zuo, Z. Advanced electrochemical energy storage and conversion on graphdiyne interface. *Nano. Res. Energy.* **2022**, *1*, 9120036. DOI
160. Liu, Y.; Xue, Y.; Hui, L.; et al. Porous graphdiyne loading CoO_x quantum dots for fixation nitrogen reaction. *Nano. Energy.* **2021**, *89*, 106333. DOI
161. Fang, Y.; Xue, Y.; Hui, L.; Yu, H.; Li, Y. Graphdiyne@Janus magnetite for photocatalytic nitrogen fixation. *Angew. Chem. Int. Ed. Engl.* **2021**, *60*, 3170-4. DOI PubMed
162. Hu, C.; Chen, X.; Jin, J.; et al. Surface plasmon enabling nitrogen fixation in pure water through a dissociative mechanism under mild conditions. *J. Am. Chem. Soc.* **2019**, *141*, 7807-14. DOI PubMed
163. Li, J.; Zhu, L.; Tung, C. H.; Wu, L. Z. Engineering graphdiyne for solar photocatalysis. *Angew. Chem. Int. Ed. Engl.* **2023**, *62*, e202301384. DOI PubMed
164. Torres-Pinto, A.; Silva, C. G.; Faria, J. L.; Silva, A. M. T. Advances on graphyne-family members for superior photocatalytic behavior. *Adv. Sci.* **2021**, *8*, 2003900. DOI PubMed PMC
165. Shandilya, P.; Mandyal, P.; Kumar, V.; Sillanpää, M. Properties, synthesis, and recent advancement in photocatalytic applications of graphdiyne: a review. *Sep. Purif. Technol.* **2022**, *281*, 119825. DOI
166. Halder, D.; Sen, S.; Roy, S. Recent advances in mechanistic studies and catalyst development for electrochemical nitrate reduction to ammonia. *Commun. Chem.* **2025**, *9*, 58. DOI PubMed PMC
167. Yin, Y.; Wang, L.; Shang, H.; Zhang, X.; Chen, W.; Zou, X. Lateral coordination sulfur-modified charge asymmetry Cu-Ru diatomic catalyst for efficient and stable electrochemical nitrate reduction to ammonia. *ACS. Nano.* **2025**, *19*, 30338-48. DOI PubMed
168. Richa, A.; Touil, S.; Fizir, M. Recent advances in the source identification and remediation techniques of nitrate contaminated groundwater: a review. *J. Environ. Manage.* **2022**, *316*, 115265. DOI PubMed
169. Yang, M.; Wang, W.; Zhao, Z.; et al. Interfacial microenvironment engineering for electrocatalytic nitrate reduction toward a sustainable nitrogen cycle. *Adv. Funct. Mater.* **2026**, *36*, e30516. DOI
170. Bai, J.; Dong, Z.; Jiang, X.; et al. Advancing nitrate-to-ammonia electrocatalysis: strategies in catalyst design, electrolyte engineering, and performance evaluation. *Adv. Sci.* **2025**, *12*, e08614. DOI PubMed PMC
171. Liu, L.; Long, Z.; Shi, K.; Zhong, H. A general crystallization picture of quantum dots: the underlying physical chemistry. *CCS. Chem.* **2025**, *7*, 926-49. DOI
172. Luo, Z.; Castleman, A. W.; Khanna, S. N. Reactivity of metal clusters. *Chem. Rev.* **2016**, *116*, 14456-92. DOI PubMed
173. Zhang, L.; Banis, M. N.; Sun, X. Single-atom catalysts by the atomic layer deposition technique. *Natl. Sci. Rev.* **2018**, *5*, 628-30. DOI
174. Yang, M.; Wang, Z.; Jiao, D.; Li, G.; Cai, Q.; Zhao, J. Tuning single metal atoms anchored on graphdiyne for highly efficient and selective nitrate electroreduction to ammonia under aqueous environments: a computational study. *Appl. Surf. Sci.* **2022**, *592*, 153213. DOI
175. Wu, Q.; Wang, Y.; Lin, D.; Li, H.; Zeng, S. Rational design of high-efficiency nitrate reduction catalysts on graphdiyne: synergistic effects in dual-active site configurations via DFT. *J. Alloys. Compd.* **2026**, *1078*, 189660. DOI
176. Zhou, X.; Tamtaji, M.; Zhou, W.; Goddard, W. A.; Chen, G. Nonprecious triple-atom catalysts with ultrahigh activity for electrochemical reduction of nitrate to ammonia: a DFT screening. *ACS. Appl. Mater. Interfaces.* **2025**, *17*, 4854-64. DOI PubMed PMC

177. Yang, L.; Feng, S.; Zhu, W. Achieving reaction pathway separation for electrochemical nitrate fixation on triatomic catalysts: a new mechanism. *J. Hazard. Mater.* **2023**, *441*, 129972. DOI